



University of  
BRISTOL

School of Chemistry

$C_2^*$  Emission from Diamond Growing  $CH_4/H_2$  Plasmas:  
Contributions from Chemiluminescent Reactions?

Joe Gore

8<sup>th</sup> April 2020

This thesis is submitted in partial fulfilment of the requirements  
for the Honour Degree of MSci at the University of Bristol

Supervisor: Professor M. N. R. Ashfold

Second Assessor: Dr C. M. Western

Third Assessor: Professor P. W. May

Section: Physical and Theoretical Chemistry

## Abstract

This project investigates several microwave-activated C/H plasmas operating at conditions relevant to diamond growth within a Microwave Plasma-Assisted Chemical Vapour Deposition (MWPACVD) reactor, employing Optical Emission Spectroscopy (OES) to probe the gas phase chemistry and inform companion plasma modelling work.

OES has a history of use in probing gas-phase reactions within C/H plasmas, especially for the reactions leading to the formation of key depositing species. Traditionally, it is assumed that the electronically excited species responsible for the observed optical emission are formed solely by Electron Impact Excitation (EIE). In order to confirm or refute this assumption, dilute CH<sub>4</sub> plasmas have been analysed as functions of parameters such as the input MW power, input CH<sub>4</sub> fraction and total gas pressure to explore the effects that changing such parameters would have on the rate of formation of excited-state species. The target species to be probed in the present work is the C<sub>2</sub> radical, which has two convenient emitting excited states – the higher energy (C<sup>1</sup>Π<sub>g</sub>), state and the lower energy and far more studied (d<sup>3</sup>Π<sub>g</sub>) states - which emit in different wavelength regions and can be monitored and compared,. Analogy with recent work on CH\* emissions from similar C/H plasmas suggests that chemiluminescent (CL) reactions (reactions that yield electronically excited products) might constitute another source of, particularly, the lower energy C<sub>2</sub>(d) products.

The present optical emission imaging study provides spatially and spectrally resolved measures of the emission intensities from the C and d states of C<sub>2</sub>, as functions of process conditions. The observed trends in these emissions, and their variations with changing process conditions, can only be accommodated by invoking an additional CL source for the d state radicals, which the companion modelling suggests is most likely within the H + C<sub>2</sub>H → C<sub>2</sub>+ H<sub>2</sub> reactions. This finding implies that, as with the CH emissions, trivial comparisons of the different C<sub>2</sub> emission intensities cannot be used as an indicator of the electron characteristics in such MW activated C/H plasmas.

## Acknowledgments

I would like to thank Doctor Ed Mahoney, who initially taught me all about the equipment and techniques. I would also like to thank Professor Mike Ashfold, without whose assistance I would not have gotten nearly this far, and for his availability and general helpfulness with any and all questions raised. Third, I couldn't have asked for greater help throughout my project from Doctor James Smith, who assisted whenever I didn't understand how and why what I was trying to do wasn't working. Finally, I would like to thank the diamond group as a whole for their general assistance, conversation and approachability.

## Abbreviations

sccm: standard cubic centimetres per minute

$F$ : flow rate

$P$ : power

$p$ : pressure

$z$ : height above the substrate

$r$ : radial distance from the centre axis of the reactor

$\chi_{CH_4}$ : methane fraction

$I_{C_2}$ : total  $C_2$  intensity

$R_I$ :  $C_2(C) / C_2(d)$  intensity ratio

CVD: chemical vapour deposition

EEDF: electron energy distribution function

EIE: electron impact excitation

HF: hot filament

HPHT: high pressure high temperature

OES: optical emission spectroscopy

OE: optical emission

REMPI: resonance-enhanced multiphoton ionization

CL: chemiluminescence

MW: Microwave

$C_2^*$ : Excited state  $C_2$

DD: Deslandres-d'Azambuja transition

## Table of Contents

<b>ABSTRACT .....</b>	<b>2</b>
<b>ACKNOWLEDGMENTS .....</b>	<b>3</b>
<b>ABBREVIATIONS .....</b>	<b>4</b>
<b>1. INTRODUCTION.....</b>	<b>6</b>
1.1 DIAMOND – A WEALTH OF NEW-AGE USES.....	6
1.2 HIGH PRESSURE HIGH TEMPERATURE GROWTH .....	7
1.3 CHEMICAL VAPOUR DEPOSITION .....	8
1.3.1 A Mention of CVD Types.....	10
1.4 DOPANTS, EXTRA SPECIES AND CONTAMINANTS.....	12
1.4.1 Boron and Silicon .....	13
1.4.2 Argon.....	14
1.4.3 Contaminants .....	14
1.5 SPECTROSCOPIC TECHNIQUES.....	15
1.6 KNOWN PLASMA REACTIONS.....	16
1.7 AIMS .....	18
<b>2. EXPERIMENTAL .....</b>	<b>18</b>
2.1 MICROWAVE PLASMA-ASSISTED CHEMICAL VAPOUR DEPOSITION (MWPACVD).....	18
2.2 OPTICAL EMISSION IMAGING.....	20
2.2.1 OES Detection Efficiencies .....	23
<b>3. RESULTS AND DISCUSSION .....</b>	<b>24</b>
3.1 DATA COLLECTION .....	24
3.1.1 Experimental Procedure.....	24
3.1.2 Metrics of Interest.....	25
3.1.3 Experimental Processing .....	26
3.2 CHEMILUMINESCENCE VS ELECTRON IMPACT EXCITATION .....	31
3.2.1 Simulations of the Plasma Chemistry and Composition .....	31
3.2.2 Electron Impact Excitation Only .....	32
<b>4. CONCLUSIONS AND FURTHER WORK .....</b>	<b>38</b>
<b>5. REFERENCES.....</b>	<b>39</b>
<b>6. APPENDICES .....</b>	<b>43</b>
6.1 MATLAB CALIBRATION .....	43
6.2 PGOPHER FITTING.....	43
6.3 EXPERIMENTAL GRAPHS .....	46
6.3.1: Spatial Profiles .....	46
6.3.2: By Process Conditions .....	48

# 1. Introduction

## 1.1 Diamond – A Wealth of New-Age Uses

Whilst hearing talk of diamond may still bring up images of rings and necklaces, an increasing range of disciplines are beginning to realize the beyond numerous applications of this very well-known crystal. With natural diamond having its price fixed at significant expense<sup>1</sup> due to the jewellery market, industrial applications are mainly focussed on working with a cheaper and less 'aesthetic' alternative – artificial grown diamond. Whilst diamond mining is still going strong at 142 million carats mined in 2019<sup>2</sup>, synthetic diamond production has risen to over 4.4 billion carats annually in 2016<sup>3</sup>, predominantly going into industrial uses, although some synthetic diamond is of sufficient purity and quality to go into traditional jewellery usage<sup>4</sup>. The primary method of this growth quality has become OES<sup>5</sup>.

The vast majority of diamond is made by one of two techniques – high-pressure high-temperature (HPHT) growth, the first available method of producing synthetic diamond<sup>6</sup>, or by chemical vapour deposition (CVD)<sup>7</sup>, (historically assumed to be mainly driven by EIE<sup>8</sup> which is starting to be refuted<sup>9</sup>), which is beginning to catch up with HPHT production<sup>10</sup> as the greater purity<sup>11</sup> and faster growth rates<sup>12</sup> available for CVD are often enough to overcome the generally higher operational cost<sup>13</sup>. In 2019, CVD diamond was responsible for around 35% of the global production, and this is projected to rise to as high as 40-45% by 2024<sup>10</sup>, especially as diamond sees even more applications driven by further research both in industrial settings and in academia.

Diamond is commonly known for being an exceptionally hard material, having a very low compressibility<sup>14</sup> of  $8.3 \times 10^{-13} \text{ m}^2 \text{ N}^{-1}$ , but it also boasts very high thermal conductivity<sup>15</sup> ( $2100 \text{ W m}^{-1} \text{ K}^{-1}$ ) and very good sound propagation velocity<sup>14</sup> ( $1.75 \times 10^4 \text{ m s}^{-1}$ ). Diamond is also very resistant to erosion by physical and chemical processes and has a wide range of very useful physical properties combined with good chemical inertness<sup>16</sup>. This lends it to a range of mechanical, electrical, thermal and optical applications, such as in cutting and drilling equipment<sup>17</sup>, heat sinks<sup>18</sup> in high-temperature electronics (due to diamond's *lack* of electrical conductivity) and other electronics such as high-powered transistors<sup>19</sup>. Other applications include windows in highly powered laser systems<sup>20</sup> and gyrotrons<sup>21</sup> due to diamond's very

low thermal expansion coefficient<sup>22</sup>. Since diamond allows for doping to be performed with relative ease<sup>23</sup>, doped synthetic diamond sees potential in several semiconducting applications<sup>24</sup> (both p-<sup>25</sup> and n-type<sup>26</sup> are possible, though n-type remains a challenge). Since high carrier mobility is also shown in CVD diamond<sup>27</sup> (up to  $4500 \text{ cm}^2 \text{ V}^{-1} \text{ S}^{-1}$ ), high-frequency electronics are also a key application of doped-diamond semiconductors<sup>28</sup>. Many other applications also exist, and are too numerous to go into here. One final potential utilization of diamond that really explores the range of usages of this simple crystal is for data storage – defects can be used to introduce or purge electrons from vacancies within the crystal structure, allowing data to be encoded and read at a later date<sup>29</sup>.

Diamond exists as a cubic covalent lattice, with a naturally octahedral unit cell with (100), (110) and (111) planes<sup>30</sup>. The carbon atoms that make up the structure are covalently bound to four other carbon atoms in  $sp^3$  hybridisation, using all 4 valence electrons and giving a very strong covalent bonding network, producing an exceptionally high atomic density<sup>31</sup> ( $3.525 \text{ g cm}^{-3}$ ) and giving rise to many of the properties previously mentioned. Diamond itself is exceptionally resistant to physical force, most commonly breaking on defect lines, impurities or grain boundaries rather than within the bulk crystal.

## 1.2 High Pressure High Temperature Growth

The origins of man-made diamond began by mimicking nature's methodology – pressure, temperature and time. The first diamond grown by HPHT was performed by Bundy and Hall<sup>8</sup> in 1955, based on previous theoretical work by Liander *et al.* in 1953<sup>32</sup>. Since diamond is denser than graphite by a good margin ( $3.51 \text{ g cm}^{-3}$ <sup>33</sup> vs  $2.26 \text{ g cm}^{-3}$ <sup>34</sup>), it is known that a high-pressure system is required to drive the phase behaviours of solid carbon to the point where diamond is favourable thermodynamically. Thermodynamically predicted conditions for HPHT growth are approximately 130 kbar and 3300 K to ensure both reliable and fast conversion, though in practice these conditions are not used to due to the challenge and expense in producing them<sup>35</sup>.

Other species can be introduced into the graphite-diamond system to act as conversion catalysts, reducing the demand for both pressure and temperature, bringing the required conditions down to a more manageable 55 kbar and 1600 K<sup>35</sup>.

At such temperatures, the common method of using such catalysts is via transition metal solutions – the metal catalyst is used as the solvent to dissolve the graphite, from which the diamond can crystallize, reducing the activation energy required for the process<sup>36</sup>. Diamond can also be generated using more extreme temperatures (~4000 K), as at this point the C-C bonds of graphite are relatively easily broken and the more thermodynamically stable state can begin to grow.

Over the time frame of diamond production by HPHT reactors, the efficiency of the specially designed reactors has been dramatically increased from initial versions. Modern reactors for this process usually employ a small compression area to generate the very high pressures required, conceptually similar to the HP reactors used for traditional inorganic operations, such as attempts to produce metallic hydrogen<sup>37</sup>. Typical materials chosen for such reactors must be very resistant to HPHT conditions, and the main material of choice is tungsten carbide, known for its extreme resistance to physical force<sup>38</sup>.

The main limiting factor of HPHT reactors is the small growing area/volume, a problem which has in part been overcome by the development of more novel methods of diamond growth, especially CVD work.

### 1.3 Chemical Vapour Deposition

Shortly after the first successful production of diamond by HPHT methods, some groups were studying diamond formation and seeding at the opposite end of the pressure scale – near-vacuum. The first successful seeding of diamond was performed by W.G. Eversole<sup>9</sup>, in which small diamonds seed onto a substrate from a heated CO gas phase.

Such methodology was termed chemical vapour deposition, which, unlike HPHT, does not operate at conditions where the thermodynamic barrier of diamond formation is overcome. Instead, CVD operates via the kinetic route – formation of diamond on surfaces maintained at a temperature of approximately 1400 K is kinetically favoured. At these conditions, the thermodynamic stability difference between graphite and diamond is very narrowly in graphite's favour, but overall, these conditions lead to favouring almost exclusive formation of diamond.

The first successful diamond growth on a surface was achieved by Spitsyn and Deryagin<sup>9</sup> in 1956, after which work was fuelled by a desire to develop low-pressure

metastable synthesis for a variety of applications, one of which was diamond growth. Hydrogen was first introduced into the gas mixture by Hibshman in 1964<sup>9</sup>, which showed hydrogen-etching of graphite and other carbon allotropes. After a period of research into the role of hydrogen, it was determined that the presence of hydrogen was H-terminating the growing surface<sup>39</sup>, which in turn increased diamond yield by reacting favourably with any present graphitic carbon, allowing it to be etched away in a reaction with hydrogen radicals, leading to volatile CH<sub>x</sub> species. These species can then undergo gas-phase reactions to form depositing species, potentially allowing them to seed back onto the surface.

The main issue of diamond CVD at that time was the poor rate of growth<sup>9</sup>, which was overcome in the 1980s by Spitsyn *et al.* through the use of substrate materials other than diamond<sup>40</sup>, and the general move to using a CH<sub>4</sub>/H<sub>2</sub> gas mixture. This gas mixture allows for a variety of gas-phase reactions, mainly via the reaction of H radicals with various carbon-containing species. After further work into the substrate, it was determined that beneficial properties include a requirement of operational stability above 900 K<sup>14</sup>, meaning that a high melting point is necessary. A significantly different thermal expansion to diamond is also highly undesirable, however the latter can be used to encourage diamond delamination from the surface after growth is complete. In accordance with these requirements, common substrates are silicon, tungsten or molybdenum, partially due to their ability to form localised carbide layers, covalently bonding to the lowest diamond layer and providing higher nucleation rates. Due to surface carbide layer formation, carbon will then not be able to diffuse into the bulk of the substrate, supporting the growth of diamond.

Also, using non-diamond substrates, the grown diamond is forced to become heteroepitaxial, forming polycrystalline diamond, divided into micro-, nano- and ultranano-crystalline diamond based on grain size<sup>41</sup>. To further increase nucleation rates, the substrate is commonly pre-processed by either abrasion with, or agitation in, a slurry containing very small diamond particles to provide a multitude of nucleation sites and increase the growing surface area as much as possible<sup>14</sup>.

### 1.3.1 A Mention of CVD Types

Several types of CVD reactor are commonly employed. The first diamond CVD reactors employed were hot filament (HF) type reactors<sup>42</sup>, where the gas mixture is initiated by the electrical heating of a heat-resistant and relatively inert metallic wire, commonly tungsten. This allows gas temperatures of 2400 K and beyond to be achieved<sup>14</sup>, though these reactor types are not without issue. One problem is the limited lifetime of the filament – which will naturally and unavoidably react with a small proportion of the input gas, leading to eventual degradation of the filament and its required replacement. Also, such reaction will reduce the resistivity of the filament, further degrading it, and will lead to some contamination of the deposited diamond by the filament material<sup>43</sup>. A final issue is the relative difficulty of probing the prevailing chemistry in the HF activated gas mixture, as due to the lack of optical emission OES is unavailable for use, leaving absorption spectroscopy and resonance-enhanced multiphoton ionization (REMPI) as the main available tool. As the activation is achieved using electrical heating of a wire, a side-effect of this is substantial levels of heat glow, essentially mimicking a very powerful filament light bulb. This means that common diagnostic techniques such as OES are very difficult to employ successfully. Such reactors, however, are generally rather cheap in comparison to other methods of producing synthetic diamond, and show respectable growth rates, so are preferably used when a large deposition area is necessary as HF can support a larger area than other techniques. Other advantages include low electrical power consumption, leading to generally cheaper running for long times than other CVD techniques, as well as the ability to grow diamond on surfaces of nearly any shape and size, a clear advantage over plasma-based CVD<sup>44</sup>.

Another relatively crude method of diamond deposition involves the use of an oxy-acetylene torch<sup>45</sup>. Generally, this method has by far the highest growth rate of any commonly-employed technique. However, it is very poor for doping studies, and generally produces the lowest-quality diamond of the major techniques. This is especially true if the flame is noticeably dirty and a large variety of other species are being produced<sup>46</sup>, though the quality is still acceptable for some uses. Similar issues in the use of diagnostic tools as with HF reactors is seen here, commonly due to how such torches are employed. Despite the difficulty in using diagnostic techniques, torches still see a generally good amount of usage due to relative ease of execution,

cost-efficiency of the equipment, high growth rates, and advances in diamond quality due to growth-etch pulsing advances<sup>47</sup>.

Diamond growth is also achievable via the use of DC-arc jet reactors, where a plasma is generated via the use of twin-torch arrangements<sup>48</sup>. One torch (P-Type) is used to generate the main body of the plasma using flows of H<sub>2</sub>/Ar, and a second torch, perpendicular to the first, is used to generate a flow of Ar plasma to stabilise the plasma before it reaches the growing surface. Carbon-containing species and dopant gases are then introduced into the plasma jet before it reaches the substrate using an injection ring. Generally, such reactors operate at a pressure of ~50 Torr and at high power, up to 10 kW in some cases. In such reactors, the substrate is inserted and held above the floor of the reactor, meaning diamond growth can only occur on the substrate surface itself<sup>48</sup>. Plasma jets allow for study of the plasma region by techniques such as cavity ring-down spectroscopy and OES, allowing good plasma diagnostics, and are very able to handle doping of the diamond surface. Issues include the very aggressive activation method used, and the far higher gas temperatures and flow rates than other reactor types meaning that some areas of plasma dynamics and plasma chemistry cannot be studied within DC-arc jet reactors. Due to the very high incident flux on the substrate, and the higher temperatures due to the high argon content, arc-jet reactors require very heavy-duty water cooling to keep the substrate at working temperatures. Also, the nozzle equipment is gradually eroded away over time, leading to similar diamond contamination issues as in HF reactors<sup>49</sup>. The small growable surface is also a major concern, as is the inability of such reactors to be viable for long-period growth due to the factors mentioned previously. As such, arc-jet reactors see limited use at this point due to advances in other reactor designs.

Our employed method of diamond CVD growth was using a microwave plasma-assisted CVD (MWPACVD) reactor. This technique involves the use of a microwave source to excite the input gas. Two main types are commonly used, the NIRIM-type reactor and the ASTEX (Applied Science and Technology Inc.) type reactors, which are shown in Figure 1, both of which operate by coupling microwaves within the chamber which contains the substrate to produce a stable plasma above the growing surface.

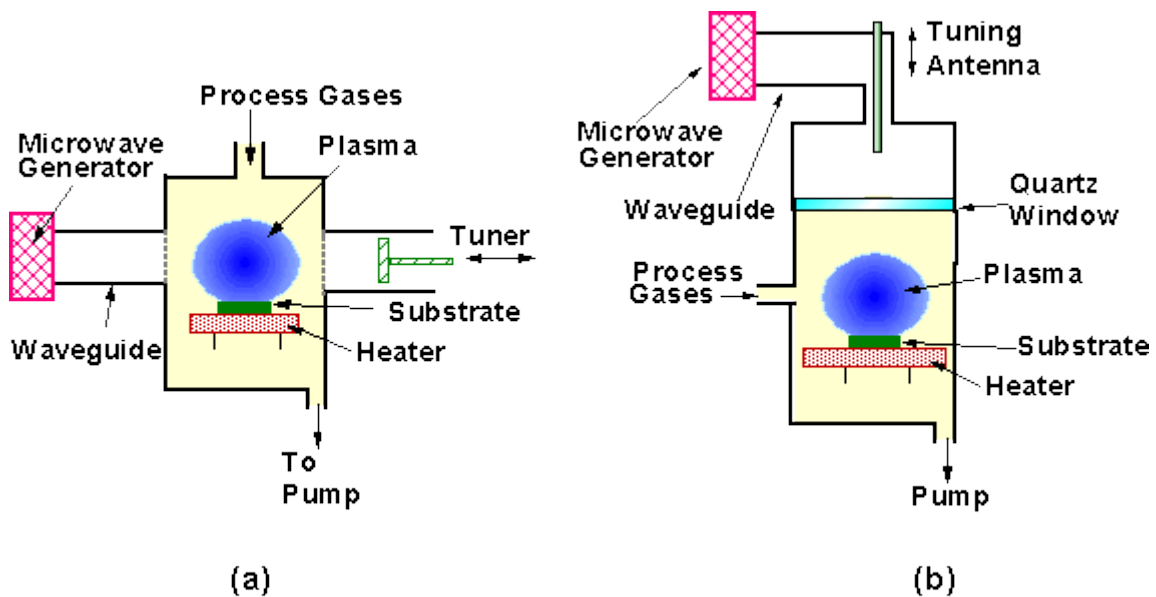


Figure 1: Schematic illustrations of (a) NIRIM and (b) ASTEX-type MW-PACVD reactors<sup>50</sup>.

The main difference between these reactor types concerns the location of the microwave waveguide, the tuning system and the direction of gas input. Most recent reactors are ASTEX-type, as the NIRIM-type reactor does not allow for independent control of substrate temperature as the plasma ball sits directly on top of the substrate, whereas in ASTEX reactors the plasma remains just above the substrate. This feature also extends to all other reactor surfaces, as in an ASTEX reactor the plasma ball sits at a distance from all surfaces, but in NIRIM reactors it can sit either very close or against a reactor surface.

These reactors benefit from the stable plasma ball that they generate, allowing for relatively easy use of many diagnostic techniques, such as OES and cavity ring-down spectroscopy, allowing a great range of studies, especially with substrate conditions<sup>51</sup>, doping<sup>52</sup>, and plasma chemistry<sup>9</sup>. The most common method of diamond growth within academia is by either HF reactors for their growth rate, ease of operation and cost-effectiveness, or in MWPAVCD reactors due to their ability to handle diagnostics and ease of varying conditions and their obvious link with most industrial CVD diamond production.

#### 1.4 Dopants, Extra Species and Contaminants

Dopants have long been identified as a way to modify a surface or solid body to add desired properties or diminish undesired ones. Arguably the primary use of dopants

in diamond systems is to produce semiconducting species, such as boron-doped diamond systems allowing for p-type semiconductivity<sup>25</sup>. Typical donor species employed have either focussed on diamond growth speed (nitrogen<sup>53</sup> and oxygen<sup>54</sup>) or the aforementioned introduction of semiconducting properties, commonly using boron<sup>55</sup> or silicon<sup>56</sup> (silicon is believed to be able to show semiconducting properties, though this is still in early stages) to introduce a band gap small enough to allow for semi conductivity. Boron can also be employed to produce p-type semiconductors due to its lower valency. n-type semiconductors are also available though they are far more challenging, primarily by doping using phosphorus<sup>57</sup> or nitrogen<sup>53</sup>.

#### *1.4.1 Boron and Silicon*

Extensive work has gone into understanding the effects of adding diborane ( $B_2H_6$ ) into the gas mixture<sup>58</sup>. This work was performed in order to better control the growth speed and quality of semiconducting diamond, whilst work into the effects of silane ( $SiH_4$ ) is in earlier stages. The addition of trace amounts of diborane to a C/H plasma has been shown to impart minimal differences on the plasma chemistry for diamond growth<sup>58</sup>, with the depositing species primarily concentrating near the surface of the substrate and gradually replacing C atoms within the surface. Due to the natural lack of boron in the air, boron contamination when it is not desired is not a concern, unless growth is being performed in a reactor which has recently been used to grow B-doped diamond. Boron can therefore only implant into the surface by either incorporating during growth or by ion implantation.

Silicon doping can occur either intentionally by adding silane to the gas mixture, or by inadvertent leaching of silicon into the plasma from the quartz windows inside the reactor, or by the usage of silicon substrates. This allows silicon to be etched into the diamond surface, and work has gone into understanding this chemistry<sup>9</sup> to minimize it where it is not desired, and control it where it is desired. Silicon incorporation, similar to boron, is not limited to etching. Silicon can be introduced via ion implantation or via incorporation during growth. However, if high levels of input silane are used, the growth of non-diamond carbon can be encouraged, potentially causing significant issues. This is another reason why significant time and effort has recently been applied to understanding H/C/Si plasmas and H/Si plasmas<sup>9</sup>.

### 1.4.2 Argon

Argon does not engage in doping as it is so fiercely unreactive. However, argon is still regularly included within C/H plasmas as it does not significantly alter plasma chemistry, but instead significantly drives up gas temperatures within the reactor since the heavier argon reduces (cf. a pure H<sub>2</sub> plasma) thermal diffusion from the hot plasma core, which gets hotter ( $T_{gas}$  and  $T_e$  both increase) resulting in more efficient thermal dissociation of H<sub>2</sub> molecules to H atoms<sup>59</sup>. Diamond growth is however only marginally affected. The current explanation for this is the increased electron temperature favouring EIE reactions, leading to vibrational excitation of H<sub>2</sub>. This leads to the dissociation of H<sub>2</sub> and C<sub>2</sub>H<sub>y</sub> species due to conversion of vibrational energy to translational energy via collisions, which drives up  $T_{gas}$  leading to a higher rate of thermal dissociation. This process usually results in the formation of a large population of acetylene (C<sub>2</sub>H<sub>2</sub>) within the plasma core. This process also causes a higher population of radical species within the plasma and increased H and C<sub>2</sub> populations, increasing growth rate.

### 1.4.3 Contaminants

By far the most common contaminant in diamond-growing reactors is an air leakage due to the sub-atmospheric pressures used. The main effect of such leaks involves the introduction of nitrogen and oxygen into the gas mixture. Nitrogen is relatively inert, but some small fraction of the N<sub>2</sub> will participate in gas phase chemistry under the prevailing plasma conditions. This will lead to the formation of CN radicals, which are easily observable by OES and serve as the main identifier of air leaks. Nitrogen, however, is very strong bonded in its native N<sub>2</sub> species, so its presence can lead to reduced gas temperatures (via absorbing some of the incident power in the form of rovibrational excitation) if the air leakage is especially bad, leading to reduced diamond growth rates and much-reduced quality of diamond grown. Oxygen, in contrast, can potentially be useful (alone, and in low concentration). Like atomic hydrogen, atomic oxygen serves to etch away non-diamond carbon from the surface and increase diamond quality, though at some detriment to growth rate. However, in the case of an uncontrolled air leak, oxygen concentrations can shift dramatically away from the 1-2% used when intentionally introducing oxygen in its atomic form<sup>54</sup>, leading to dramatic reductions in growth rate due to increased surface etching. As oxygen is also reactive with the input CH<sub>4</sub>, leading to the formation of non-reactive

CO, the effects of adding atomic oxygen are also dependant on the CH<sub>4</sub> mole fraction.

The main other concern involves the etching of any deposited carbon into the walls of the reactor as well as the evaporation of minute amounts of the walls and floor of the reactor itself. This can lead to minor contamination by both copper and iron (from the floor and walls of the reactor respectively) in the as-grown diamond. Also possible is the excess of carbon caused by this forming a graphitic layer on the diamond surface, which is a relatively minor concern though one that must be considered.

### 1.5 Spectroscopic Techniques

Whilst a multitude of diagnostic techniques into gas-phase reactions and activity are known to be applicable to diamond-growing plasmas, only OES was used as it served to fulfil the required needs of this time-limited project. Other techniques that have been applied in studies of activated gas mixtures for diamond CVD include Cavity Ring-Down Spectroscopy (CRDS)<sup>60</sup>, REMPI<sup>61</sup>, Infrared (IR) absorption<sup>62</sup>, Raman spectroscopy<sup>63</sup> and Mass Spectrometry (MS)<sup>64</sup>. These techniques were not available for the current project and, even if they had been, it is arguable what additional information they might have provided. MS would only have assisted us in viewing non-emitting carbon containing species, which were unnecessary for this project. IR would not have allowed us to observe the C<sub>2</sub> as there is no change in dipole moment on vibration of C<sub>2</sub>. As such, OES alone was deemed necessary to fulfil the requirements of this project.

OES has risen to become *the* non-invasive plasma diagnostic tool of choice within diamond-growing CVD plasmas and allows for the identification and distinction of key C<sub>2</sub>, C<sub>2</sub><sup>-</sup>, CH and atomic emission lines. Notable emission lines of C<sub>2</sub> include the d<sup>3</sup>Π<sub>g</sub>-a<sup>3</sup>Π<sub>u</sub> (Swan) transition<sup>65</sup>, which has been used extensively as the main indication of C<sub>2</sub> presence and population within diamond-growing plasmas<sup>66</sup>. Also present, though far less intense, is the C<sup>1</sup>Π<sub>g</sub>-A<sup>1</sup>Π<sub>u</sub> (Deslandres-d'Azambuja [DD]) band<sup>67</sup>, a system which has been commonly ignored due to the presence of the Swan band in a more convenient wavelength range, which possesses a far higher intensity and allows for the observation of satellite bands (i.e. transitions involving a change in vibrational quantum number (v) in tandem with the electronic state

change). Key atomic lines identifiable include the hydrogen Balmer series, which, whilst not important for this work, is a useful visual tool to check for degradation and contamination of the plasma<sup>68</sup>. The CN  $B^2\Sigma^+-X^2\Sigma^+$  transition is also visible in the operation range of the spectrometer and allows a very sensitive visual identifier for any air leakage into the reactor, ensuring that data is collected in ideal conditions.

OES is a reasonably straightforward technique that allows probing the electronically excited species<sup>69</sup> (formed via EIE and, in principle, CL reactions) within the plasma without causing any perturbations to the plasma system.  $T_{gas}$  is often determined using OES, as laser pyrometry is unfeasible due to the large number of discrete wavelength emissions produced from the plasma. OES has been extensively employed within this reactor previously, primarily to observe excited state H, H<sub>2</sub>, CH, C<sub>2</sub> species and simple silicon-containing species (like Si, SiH etc), with typical variations in conditions including  $P$ ,  $p$ , gas flow (H<sub>2</sub>, SiH<sub>4</sub>, CH<sub>4</sub>, Ar, etc), substrate diameter, spacer wire diameter (the variation of which can moderate the substrate temperature) and substrate material.

Analysis of the C<sub>2</sub> Swan band has historically been used as a proxy for the total carbon content of the plasma<sup>65</sup>, and has been used (via Boltzmann plots) to provide some measure of rotational temperature, which has been assumed equal to the gas temperature due to the high collisional rate and efficiency at such conditions. Since EIE was assumed to be highly dominant at these conditions<sup>2</sup>, OES outputs have also been used as a direct probe for the electron temperature within the reactor, potentially leading to false conclusions in historical work under conditions where, as shown in the previous work<sup>3</sup>, EIE is not the only sources of the emitting species.

### 1.6 Known Plasma Reactions

Almost all diamond CVD employs a dilute CH<sub>4</sub> source gas mixture. CH<sub>4</sub> is relatively inexpensive and is available in high purity. The activated gas mixture supports numerous H-shifting reactions – shown in Figure 2 – which have the net effect of converting most of the input CH<sub>4</sub> into C<sub>2</sub>H<sub>2</sub> within the hot plasma region. These C<sub>2</sub>H<sub>2</sub> molecules are in local equilibrium with lesser concentrations of C<sub>2</sub>H and C<sub>2</sub> radicals. The latter are the target of the present study. As noted previously, the H atoms required to drive these H-shifting reactions arise via the reaction of hydrogen, which is vibrationally excited by EIE (reaction (1.1)). Collisions involving these vibrationally

excited H<sub>2</sub> molecules can then lead to thermal dissociation and generation of hydrogen atoms<sup>70</sup>.



These hydrogen radicals can then undergo a series of reactions (shown in Figure 2) to form acetylene from methane, which itself is in equilibrium with other C<sub>2</sub>H<sub>y</sub> species, including C<sub>2</sub>.

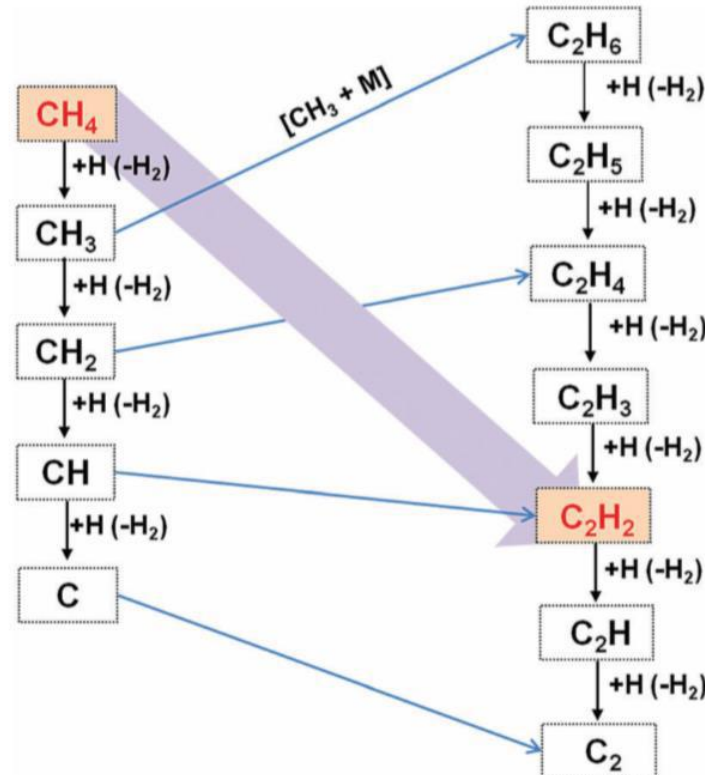


Figure 2: A diagram of the H-shifting reactions of the C<sub>1</sub> and C<sub>2</sub> hydrocarbon species within the plasma core<sup>9</sup>.

These reactions are dominant within the hottest regions of the plasma, occurring directly above the substrate surface<sup>9</sup>. The current understanding of these processes is that hydrogen loss reactions predominate within the hot plasma regions, after which recombination can occur closer to the reactor walls to form the C<sub>2</sub>H<sub>y</sub> species. These species can then undergo further hydrogen loss, though >95% of all carbon within the plasma region remains as C<sub>2</sub>H<sub>2</sub>. It is known that the dominant carbon-containing species within the plasma core include CH<sub>x</sub> (x<4), C<sub>2</sub>H<sub>2</sub>, C<sub>2</sub>H and C<sub>2</sub>, with species such as methane tending to collect in the cooler regions (e.g. near the reactor walls). Whilst C<sub>2</sub> is a relatively minor species within the plasma core, it

happens to emit very strongly and has two excited states which are very useful for this study, so this is the main species we focus on observing.

### 1.7 Aims

The main aim of this thesis is use of OES methods to investigate the relative importance of EIE and CL sources in the formation of C<sub>2</sub> radicals in their excited d and C states and analysing OE images recorded centred at 530 and 410 nm, respectively. The intention is to inform an update to an existing simulation<sup>9</sup> which will result in an improved set of reactions and reaction rates to explain and interpret OE measurements of C/H plasmas under a wider range of process conditions. The present experimental data clearly shows that EIE cannot be the sole source of, particularly, C<sub>2</sub>(d) radicals. As with the recent OE imaging study of CH emissions from similar C/H plasmas<sup>3</sup>, the recognition that CL reactions contribute to the production of the most commonly monitored excited states of both C<sub>2</sub> and CH radicals in MW activated C/H gas mixtures raises further question marks as to what is the simplest robust route to exploring electron characteristics in such plasmas.

Within this report, Chapter 2 will outline the experimental apparatus, spectroscopic and data collection methods used - before proceeding to the results and their discussion in Chapter 3, and concluding in Chapter 4 with an overview of the key findings and suggestions for further work.

## 2. Experimental

### 2.1 Microwave Plasma-Assisted Chemical Vapour Deposition (MWPACVD)

All experimental work was performed in a custom ASTEX-type MWPACVD reactor (Figure 3) to generate microwave-activated C/H plasmas.

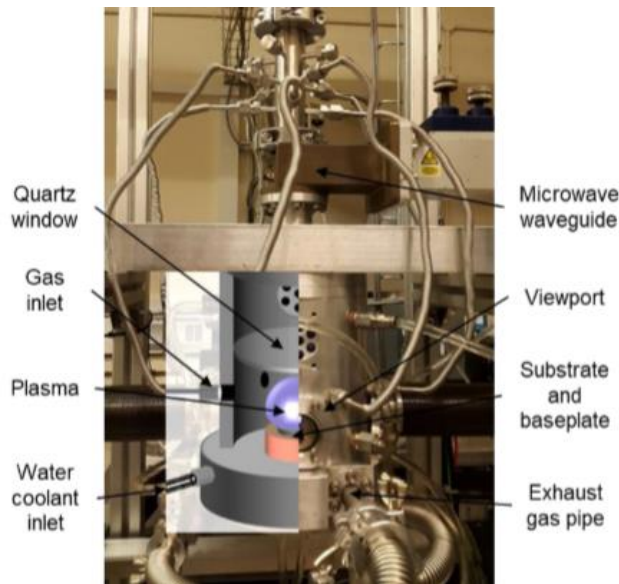


Figure 3: A split diagram of the custom ASTEX-type reactor used in this study<sup>3</sup>, shown as a photograph (right half) and a cut-away image (left half).

Microwave powers up to 2 kW can be supplied, produced by a 2.45 GHz Muegee generator. This microwave radiation is passed through a rectangular waveguide and a set of three tuning forks, converting into the  $TM_{01}$  mode, allowing the microwaves to couple into a standing wave within the reactor chamber. The reactor chamber is a vertically aligned cylinder, with an internal diameter of 12 cm, and a quartz window separating a lower deposition chamber of approximate volume  $600 \text{ cm}^3$ . This bottom chamber is vacuum sealed and holds the plasma and substrate when in use. The tungsten substrate (32 mm diameter, 3 mm thick) sits on a 0.01-in. thick molybdenum spacer wire which in turn sits on an oxygen-free water-cooled copper sample stage, mounted within an aluminium alloy base plate. The top section of the cylinder is open to the atmosphere, through which air is vented whilst the reactor is in use to keep the quartz window cool.

The source gases are separately metered, allowing fine control of flow rates in standard  $\text{cm}^3$  per minute (sccm) through individual mass-flow controllers. These gases are then mixed and flowed through a single pipe to homogenise the input gas. This flow is then split evenly between two diametrically opposed 4mm diameter inlet pipes below the quartz window, giving cylindrically symmetric gas input into the reactor. The source gases are then vented through the baseplate. The standing microwaves within the lower chamber will then activate the gas mixture, generating all the species shown in Figure 2.

Base conditions of the reactor are consistent with previous work<sup>3</sup>, operating at flow rates  $F(\text{H}_2) = 300$  sccm,  $F(\text{CH}_4) = 19$  sccm, pressure  $p = 150$  Torr, applied MW power  $P = 1.5$  kW. The plasma is produced by first setting the reactor to  $F(\text{H}_2) = 300$  sccm and  $p = 20$  Torr, where the plasma is initiated by the microwaves, after which the reactor was steadily brought up to full base conditions. Feasible operable ranges for the varied conditions typically lie within the ranges of  $0 \leq F(\text{CH}_4) \leq 20$  sccm,  $50 \leq p \leq 275$  Torr,  $0.7 \leq P \leq 1.85$  kW, whilst maintaining all conditions other than the one being varied at the base values.

## 2.2 Optical Emission Imaging

OES was performed using an Andor SR-500i Czerny-Turner spectrograph, with a 500 mm focal length  $f/16$  objective lens. Plasma emissions pass through the rear reactor viewport and through a 10  $\mu\text{m}$  wide entrance slit into the spectrograph, where the radiation is collimated, reflected by a 700 lines/mm diffraction grating and focused onto an Andor Newton 940 CCD array detector. The grating used was an MKS 53\*-455R, operating with 700 lines/mm and a nominal blaze wavelength of 530 nm, with a blaze angle of  $10.5^\circ$ . The CCD is cooled to  $-60$   $^\circ\text{C}$  when in use to filter out background current and limit pixel saturation. The spectrograph is positioned so that the emissions from the centre of the plasma are focussed onto the CCD, with the front viewport of the reactor covered with a non-reflective card during measurements, and all external lighting removed to limit any background signal. In each run, accumulation time was set to 30 seconds, and 10 accumulations were taken for a total time of 5 minutes.

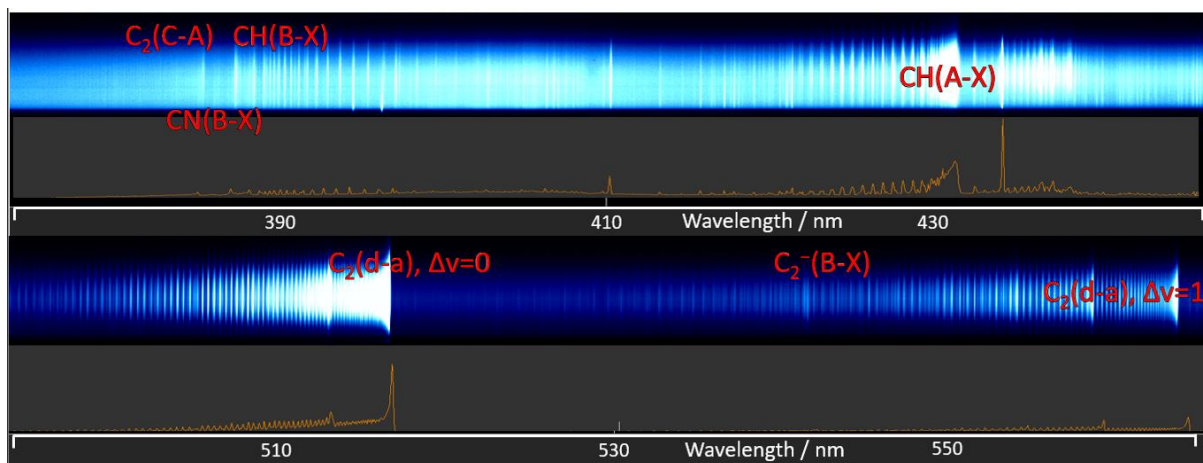


Figure 4: A sample view of the OES output at both wavelength ranges.

Andor Solis software was used to view and process the OES output, which allowed for immediate visual inspection of the accumulations to check for emissions from species of interest and signs of excessive air contamination (via CN emissions). In images such as those shown in Figure 4, the y-axis represents height above the substrate (traditionally labelled as  $z$ , where  $z = 0$  defines the substrate surface), while the x-axis shows the wavelength. Images were spatially calibrated by imaging a card with alternating 3mm wide black and white horizontal stripes, placed at the centre of the reactor, against which the later runs were calibrated and de-skewed. This calibration and de-skewing were performed using MATLAB, which was also used to produce spatial profiles, binned in either 20 sets, 1.5 mm in height or in 10 sets, 3 mm in height.

The relevant emissions for the present experiments were the  $C_2$  Swan band, with electronic origin at 516 nm, the  $C_2$  Deslandres-d'Azambuja band, the prominent band head of which appears at 385 nm, the CH(B-X) band, headed at 387 nm and the  $C_2^-$  Herzberg-Lagerqvist band, which shows a band head at 541.6 nm. All these bands are labelled in Figure 4. The  $C_2$  Swan band emission in the present experiments was monitored via the  $\Delta v = +1$  (i.e. the  $v' \rightarrow v'' = v' + 1$ ) sequence rather than the more intense  $\Delta v = 0$  progression to allow the  $C_2^-$  system to also be analysed in the same spectrum. The  $C_2$  Deslandres-d'Azambuja system, the other emission of particular interest in this work was monitored via its  $\Delta v = 0$  sequence, which allows the CH(B-X) system to be analysed in the same spectrum, and any CN(B-X) emission to be monitored visually to check for air contamination. The CH(B-X) system in question is the  $B^2\Sigma^- - X^2\Pi$  transition, and the  $C_2^-$  transition is the  $B^2\Sigma^+_{u-} - X^2\Sigma^+_{g}$  transition. Further details of the constants used for these states and transitions are shown in Table 1. For each set of conditions, 2 accumulations were taken, one centred at 530 nm, to image the Swan band, and another centred at 410 nm to image the Deslandres-d'Azambuja band. Many atomic peaks are also visible in the spectrum. By far the most intense of these are the hydrogen Balmer lines and the atomic peaks of iron and copper. Iron and copper are present due to small amounts leaching off from the walls and floor of the reactor respectively. Hydrogen Balmer lines are present due to the population of electronically excited H atoms, which are formed from EIE induced thermal dissociation of  $H_2$  and subsequent thermal dissociation of the resulting ground state H atoms. These peaks can then be used as

a guide against which to estimate the relative populations of the carbon-containing species, allowing for a visual comparison of total carbon population between runs against hydrogen. The most prevalent of these lines is the Balmer  $\gamma$  line visible in the upper panel of Figure 4 at 434 nm.

Constant	Units	$d^3\Pi_g$	$a^3\Pi_u$	$C^1\Pi_g$	$A^1\Pi_u$
$T_{elec}$	$\text{cm}^{-1}$	20022.5	716.2	34261.3	8391
$\omega_e$	$\text{cm}^{-1}$	1788.22	1641.35	1809.1	1608.35
$\omega_e X_e$	$\text{cm}^{-1}$	16.440	11.67	15.81	12.07
$\omega_e Y_e$	$\text{cm}^{-1}$	-0.5067	-	-	-0.01
$B_e$	$\text{cm}^{-1}$	1.7527	1.6324	1.7834	1.613
$\alpha_e$	$\text{cm}^{-1}$	0.01608	0.1661	0.018	0.0168
$\gamma_e$	$\text{cm}^{-1}$	-0.001274	-	-	$-5.4 \times 10^{-5}$
$D_e$	$\text{cm}^{-1}$	$6.7 \times 10^{-6}$	$6.44 \times 10^{-6}$	$6.8 \times 10^{-6}$	$6.44 \times 10^{-6}$
$\beta_e$	$\text{cm}^{-1}$	$1.03 \times 10^{-7}$	-	-	$3.6 \times 10^{-7}$
$r_e$	Å	1.2661	1.3119	1.2552	1.3184
$T_r$	-	d-a	N/A	C-A	A-X
$\nu_{00}$	$\text{cm}^{-1}$	19378.44	N/A	25969.19	8268.16

Table 1: Molecular constants of  $C_2$  in the relevant states to this work<sup>71</sup>, where  $T_{elec}$  = minimum electronic energy,  $\omega_e$  = first vibrational constant,  $\omega_e X_e$  = second vibrational constant,  $\omega_e Y_e$  = third vibrational constant,  $B_e$  = equilibrium rotational constant,  $\alpha_e$  = first rotational constant,  $\gamma_e$  = rotation-vibration interaction constant,  $D_e$  = centrifugal distortion constant,  $\beta_e$  = first centrifugal force rotational constant,  $r_e$  = internuclear distance,  $T_r$  = primary observed transition and  $\nu_{00}$  = position of 0-0 band for the primary transition.

The collected accumulations were fit against two simulated spectra in PGOPHER, at a scale of  $1e-8$  and using a 4<sup>th</sup> order polynomial intensity correction to correct for any long-range variations in the baseline. PGOPHER was operated using a fixed gaussian linewidth value, with the concentrations of the species of interest and the total gas temperature allowed to float to improve the fitting of the simulation. In order to fit the spectrum, PGOPHER uses provided data about the simulated band systems (data sourced from Mentall and Nicholls<sup>72</sup>. and with the integrated transition intensity adjusted by a factor of 2.2 to replicate the lifetime of  $C_2(d)$  reported by

Brooke and Bernath *et al.*<sup>73</sup>) to replicate a spectrum, then allows the gas temperature and populations of the emitting state of interest. The integrated area under the peaks of interest were then taken as the relative intensity of the band, which allowed for comparisons between band systems and for quantifying changes in any one band system with changes in process conditions. A sample fitting process for illustrative purposes is shown in the appendix (section 6.2).

### 2.2.1 OES Detection Efficiencies

One potential effect which could dramatically alter the results if not addressed is the efficiency of both the grating and the detector at the wavelengths in question (410 nm for C<sub>2</sub>(C), 530 nm for C<sub>2</sub>(d)).

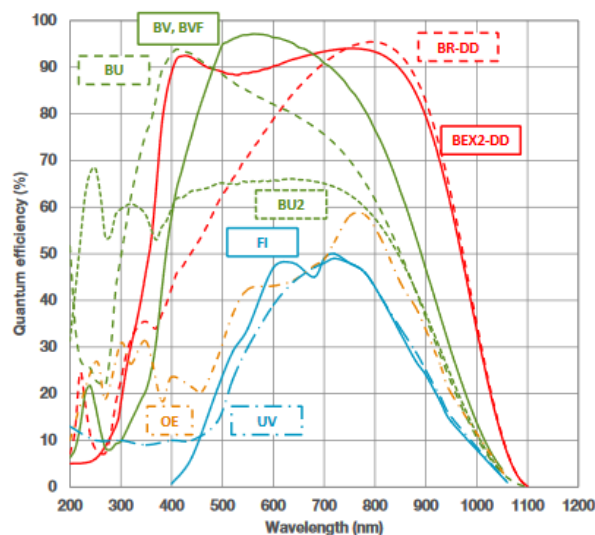


Figure 5: A graph of the efficiency of the CCD against wavelength<sup>74</sup>.

As Figure 5 shows, the efficiency of the BU2 CCD in the existing spectrometer is roughly equal at these wavelengths, with an overall efficiency of approximately 64%. As such, no correction must need be applied based on the detection efficiency of the CCD.

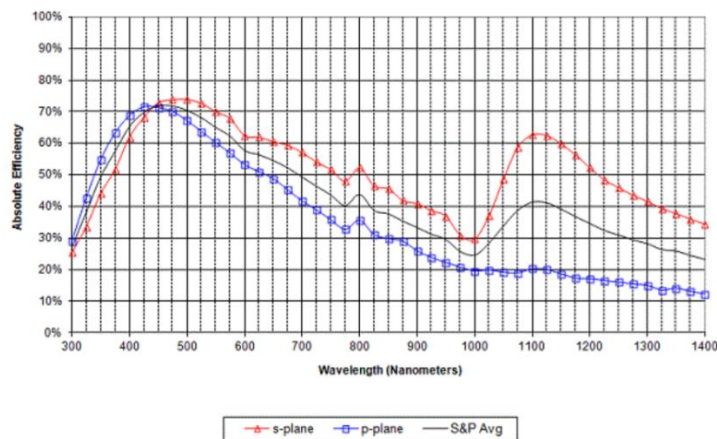


Figure 6: A graph of the efficiency of the grating against wavelength<sup>75</sup>.

Figure 6 shows that the same is true of the grating employed, with only a minor overall effect on the efficiencies of observing the two species, a difference of roughly 3% efficiency between 410 nm and 530 nm in the average of the s- and p-polarised reflectivity. Overall, no correction needs to be applied to the values collected to address any dramatic difference in the efficiency of the CCD or the grating at the wavelengths in question.

### 3. Results and Discussion

#### 3.1 Data Collection

##### 3.1.1 Experimental Procedure

To establish experimental conditions,  $F(\text{H}_2) = 300$  sccm was introduced to an evacuated reactor and the pressure allowed to build to 20 Torr. The microwave generator was then turned on at approximately 0.5 kW to “strike” an initial plasma ball over the substrate. The tuning forks were then utilized to adjust the reflected power ( $P_{ref}$ ) to as close to zero as possible. The pressure was then steadily increased to 150 Torr, with  $P_{ref}$  being continually minimized. Once  $p = 150$  Torr had been reached, the power was adjusted to  $P = 1.5$  kW. During this adjustment,  $P_{ref}$  also rises, but was always maintained well below 0.1 kW until the adjustments were completed, then further minimized once 1.5 kW was reached. After this, methane was flowed in at  $F(\text{CH}_4) = 19$  sccm and the tuning forks were again used to minimize  $P_{ref}$ . After this point, further adjustments could be performed. In the case of data sets 3.1.1 and 3.1.2, the tuning forks were left untouched throughout the data collection,

while for data set 3.1.3 it was necessary to adjust the tuning forks to keep the plasma stable and productive.

Collected optical images were first calibrated in MATLAB (as detailed in appendix 6.1) to establish a consistent baseline and the data then binned into  $z = 1.5$  mm or 3 mm wide strips, for ease of processing and comparison. The calibrated images were then fitted against the relevant PGOPHER simulation (detailed in appendix 6.2) to give population/intensity information about the species of interest.

### 3.1.2 Metrics of Interest

The ratio  $R_I$ , (defined in the abbreviations section as the ratio of the  $C_2(C-A)$  to  $C_2(d-a)$  emission intensities recorded under any given set of process conditions), its spatial variation under these process conditions, and its variation with changes in process conditions are all of special interest and are one of the main outputs of this study. The absolute and relative  $R_I$  values are used to inform the simulation work performed by collaborator Dr Yuri Mankelevich (Moscow State University) that is briefly summarized in section 3.2.3. These values have also been used for display purposes in the present work, to scale the DD band intensities up to those of the Swan band emissions, which is achieved by averaging  $R_I$  at every point in an experimental set and then scaling every DD band point by this average.

The rotational temperature ( $T_{rot}$ ) returned by the spectral simulations and taken as a proxy for the gas temperature  $T_{gas}$  was used to check the validity of any fits to measured spectra. Here it is important to recognise that the monitored emission is from the whole depth of the plasma, so includes contributions from both the hottest core region and the somewhat cooler periphery of the plasma ball. So, although  $T_{gas}$  is predicted to be  $> 3000K$  in the core of the plasma, it is unlikely to be this high in any simulation of OE from plasmas operating at the base pressure and power conditions. Similarly, any simulation that returned  $T_{rot} < 2000K$  would give cause for concern as gas temperatures below this within the luminous plasma region are highly unlikely.

The experiments only sample a fraction of the total excited state emission (eg in the case of the Swan bands, we choose only to monitor the  $\Delta v = +1$  sub-band). Intensity information from the PGOPHER simulation is typically in arbitrary units (though this can be made absolute if/when the quantitative transition strength information is

available). Furthermore, the returned emission intensities (whether relative or absolute) do not correspond directly to excited state populations – the determination of which requires further information about transition probabilities (Einstein A coefficients), excited state quenching probabilities and instrumental factors such as the relative detection efficiencies at the wavelengths in question. In general, the main focus of the present work is on comparative measurements between the Swan and DD bands, so the aforementioned issues with the absolute emission intensities are minor concerns due to the consistent data collection methods employed. Such methods included a wait time of 6 minutes (equivalent to 3 residence times) between each change in conditions to allow for sufficient gas exchange between collections, identical spectral ranges for each collection at each wavelength centring and identical data collection times of 5 minutes (a series of  $10 \times 30$  second long accumulations, then averaging) for each OE image.

### 3.1.3 Experimental Processing

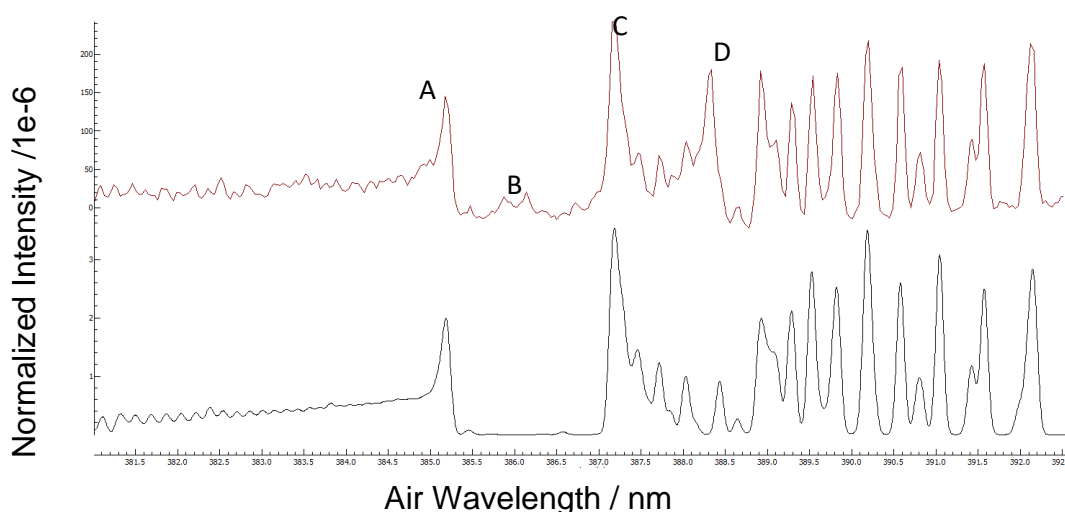


Figure 7: A graph of the experimental (red) and simulated (black) spectra when viewing at a centre wavelength of 410 nm at base conditions.

Figure 7, the red trace, which was taken at base conditions, is an example of how the spectra centred at 410 nm were fitted in PGOHPER to give relative populations. In this spectrum, peak A is the band head of the DD band, peak B is CN(B-X) and peak C is the CH(B-X). Only the DD and CH(B-X) bands were included in the PGOPHER simulation (shown in black). The CN(B-X) band was not included in the simulation, and the intensity of this band was used as previously mentioned as an

indicator of air leak – if the CN peak was approximately half the height of the CH(B-X) peak or above then the collection would have to be repeated. The peak labelled D is the only significant feature in the experimental spectrum which is not reproduced well in the simulation, it is assigned to atomic tungsten originating from the substrate.

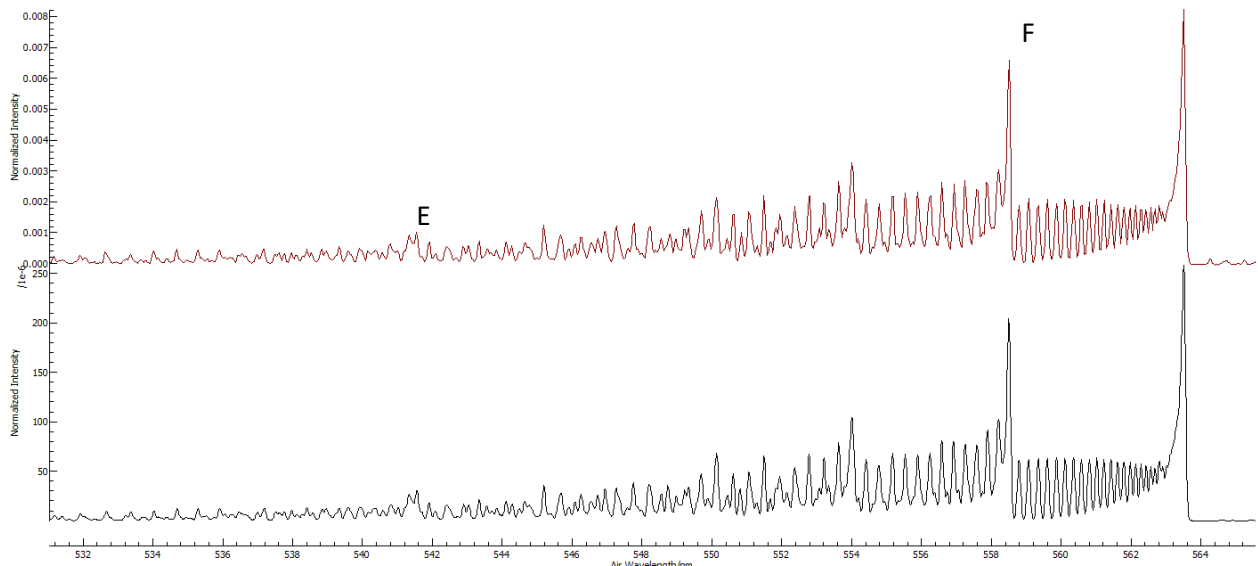


Figure 8: A graph of the experimental (red) and simulated (black) spectra centred at 530 nm at base conditions.

Figure 8 illustrates how the spectra centred at 530 nm were fitted. Peak E is the peak for the  $C_2^-(B-X)$  system, whilst peak F is the band head for the main  $v'=0 \rightarrow v''=1$  transition in the  $\Delta v = +1$  system of the Swan band. The fitting at this wavelength is very good due to the higher amount of information available about this band system due to the extensive studies performed on it, meaning the fitting is significantly better. There are also no major atomic bands in this range, meaning there nothing to deviate significantly from the simulation.

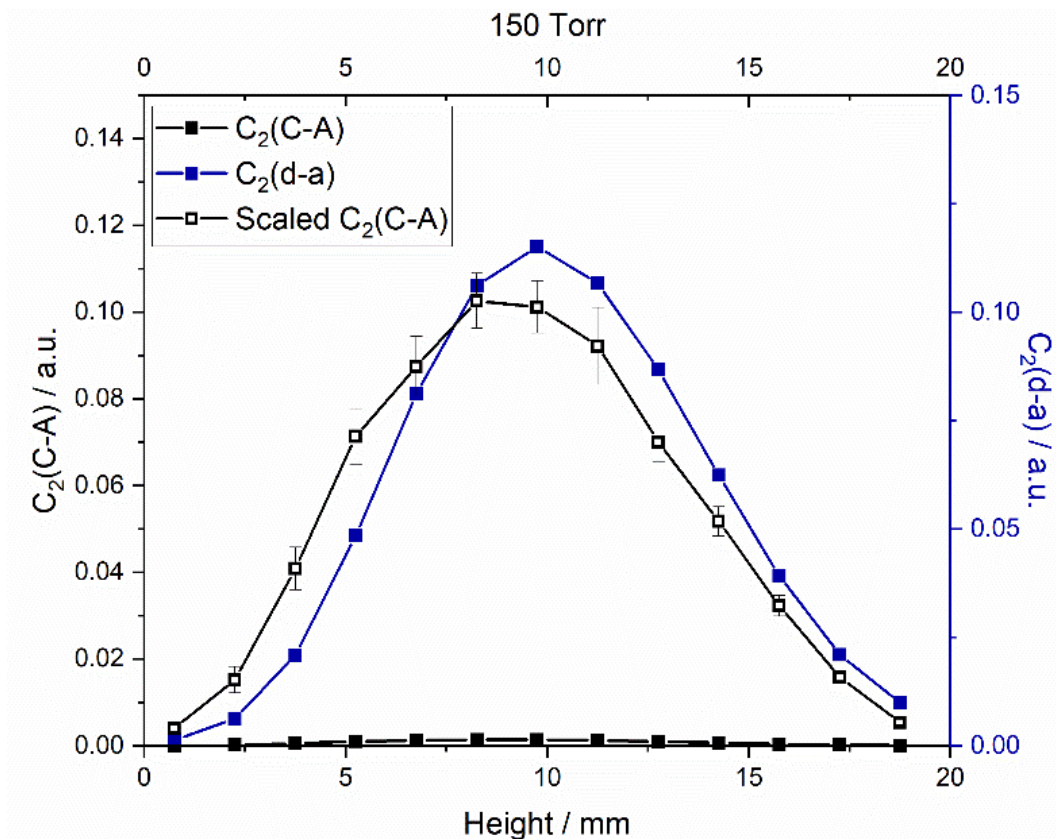


Figure 9: A graph showing the  $z$ -dependency of the Swan and DD emission intensities recorded at base conditions.

As shown in Figure 9, the two emissions show noticeably different spatial (by  $z$ ) profiles. Scaling for the DD band intensities was performed by the method detailed in section 3.1.2. The DD emission peaks at lower  $z = 7.5$  mm and tails off faster than the Swan band emission (peaking at  $z = 10.5$  mm) consistent with the higher  $T_e$  required to excite the higher energy C state - and is overall far less intense at all points due to the lower emissivity and lower population of the C state. Both emissions are weak very close to the substrate (where substrate-gas interaction dominate) and at high  $z$ , where electron density and the  $T_e$  are both substantially lower, and the plasma is not present, and so the concentration of excited state carbon radicals becomes much lower. Both emissions peak near the centre of the plasma ball, where the population of hydrogen and carbon-containing radicals is high, and where the  $T_e$  is high - as has been shown before for a range of emitting radical species<sup>9</sup>.

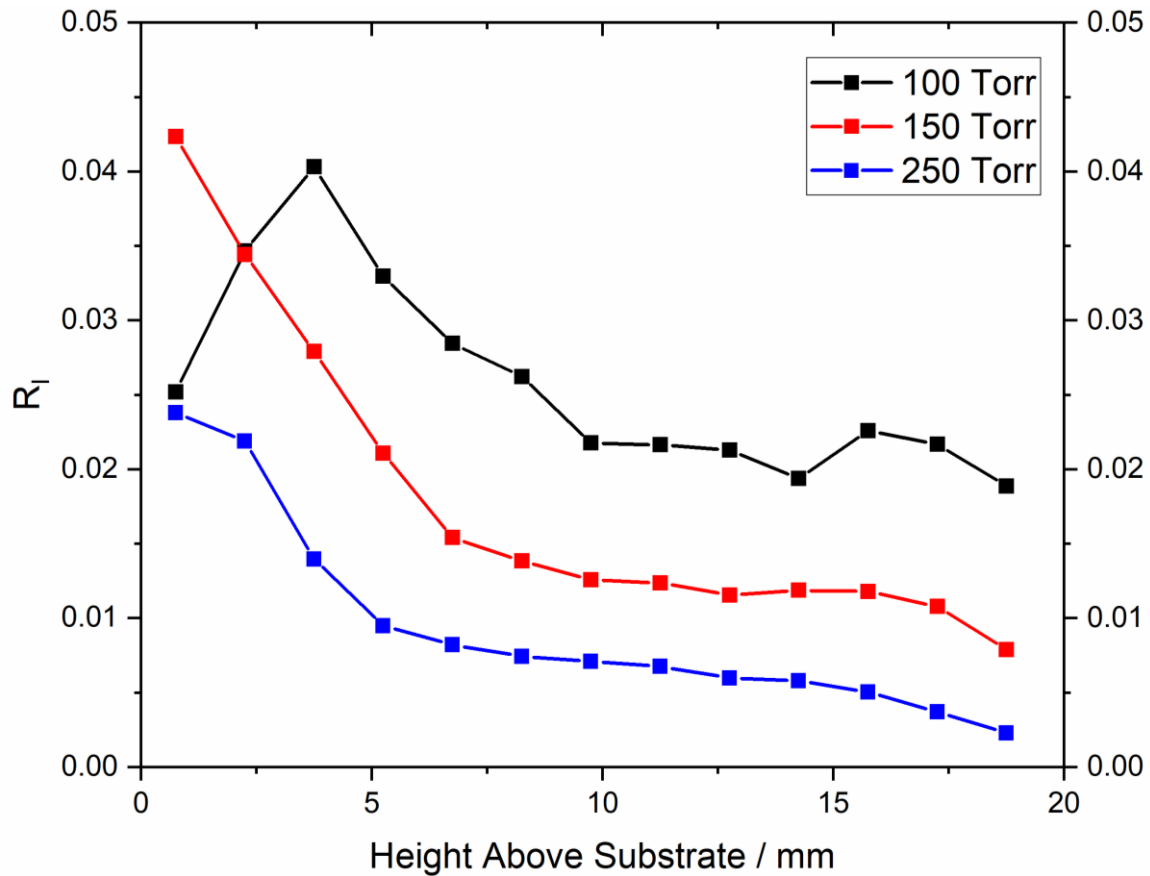


Figure 10: Plots of  $R_I$  vs  $z$ , for three different  $p$ , with  $P$  and  $\chi_{CH_4}$  maintained at their base values.

As  $z$  increases,  $R_I$  is observed to decline, as shown in Figure 10. This decline is fast at first, dropping by approximately 50% from  $z = 0 - 5$  mm, then tails off more slowly with increasing  $z$ . At  $z = 0.75$  and  $18.75$  mm, the signal-to-noise ratio is so low that the error is on the order of 200% or more (this can be seen more clearly in the spatial plots, shown in section 6.3.1), so points shown at such heights are for illustrative purposes only and do not necessarily indicate any drop or rise in  $R_I$  at very low or very high  $z$ . As pressure is increased,  $R_I$  decreases, which is not what might be expected with an EIE-only picture, for which, little if any dependency on  $R_I$  ratio would be expected. Excited state quenching would be expected to show a pressure-dependence, but a model based on EIE as the source of  $C_2^*$  species and allowing differential quenching of d and C state  $C_2^*$  radicals can reproduce the differences in  $R_I$  with  $p$ , but not the steep decline in  $R_I$  at small  $z$ . The increase of the emission intensity of both  $C_2$  states as a function of process conditions can be seen in appendix 6.3.2.

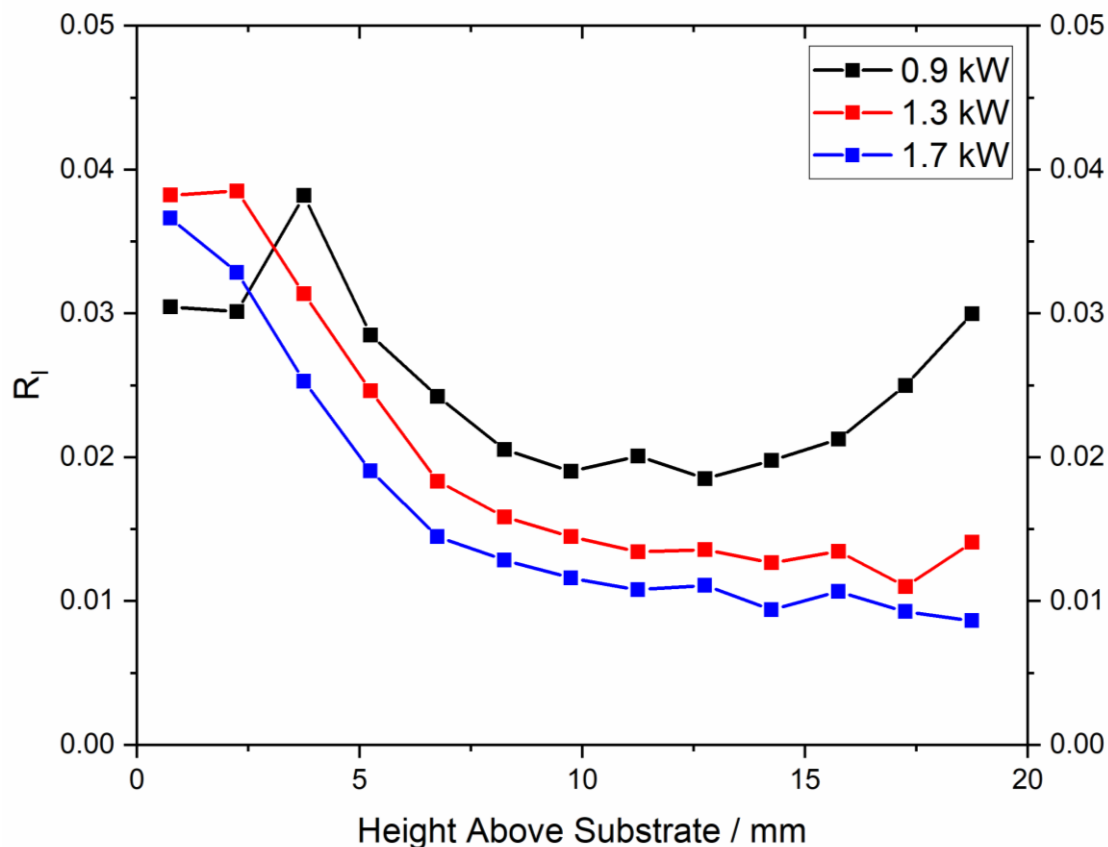


Figure 11: Plots of  $R_I$  vs  $z$ , for three different  $P$ , with  $p$  and  $\chi_{CH_4}$  maintained at their base values.

Figure 11 shows analogous plot to Figure 10, but for three different MW powers instead of pressures. Figure 11 demonstrates the same spatial profile as Figure 10, again with an approximate decay of 50% between  $z = 0 - 5$  mm. As the power is increased,  $R_I$  is again shown to decrease, indicating preferential formation of d state  $C_2^*$  radicals, which is not predicted by EIE alone but could be accommodated by an EIE source plus excited state selective quenching rates.

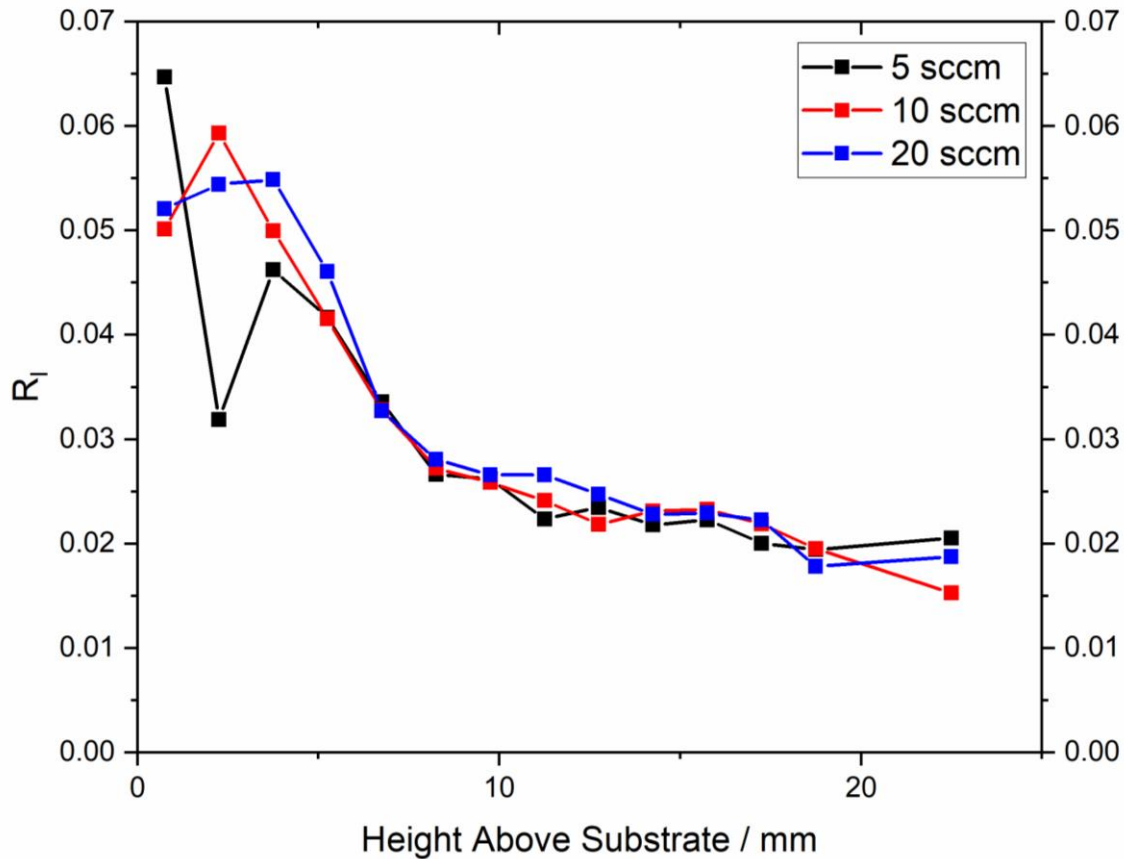


Figure 12: Plots of  $R_l$  vs  $z$ , for three different  $\chi_{CH_4}$ , with  $p$  and  $P$  maintained at their base values.

The methane mole fraction dependence of  $R_l$  is shown in Figure 12, again plotted as a function of  $z$ . In contrast to Figures 10 and 11, changing  $\chi_{CH_4}$  has little to no effect on  $R_l$ . This is what would be expected for all 3 process conditions if EIE was the only production mechanism of  $C_2^*$ , however it is only shown for one of the variables:  $\chi_{CH_4}$ . The same spatial profile is shown again, giving us no reason to doubt any of the results. This meant that we could go ahead and use this information to produce new simulations to test the historical assumption that EIE was the sole production mechanism for  $C_2^*$ .

### 3.2 Chemiluminescence vs Electron Impact Excitation

#### *3.2.1 Simulations of the Plasma Chemistry and Composition*

The simulation used was a 2-D ( $r, z$ ) model of the MWPACVD reactor, which is entirely self-consistent and is labelled as [C2-2020], an update based on previous models<sup>9</sup>. The changes as compared with previous models include specific production/loss mechanisms for the  $C_2(d)$  and  $C_2(C)$  states. Overall, the model

covers roughly 340 reactions and 40 species that are present within the reactor, and works with electron kinetics, heat and species transfer, gas-surface interactions, spatial-dependant MW electromagnetic fields and MW power absorption within the plasma. Electron energy distribution functions (EEDFs) are calculated in all cells of the (r, z) grid from Boltzmann equation solutions with the use of e-H, e-H<sub>2</sub>, e-C<sub>x</sub>H<sub>y</sub>, ( $x \leq 2$ ,  $y \leq 6$ ) and e-ion collision cross sections, where e is used as short hand for electron.

### 3.2.2 Electron Impact Excitation Only

The analysis began on the basis that the traditional assumption was correct; that electron impact excitation (EIE) was responsible for all C<sub>2</sub><sup>\*</sup> emission from the plasma core. To this end, the simulations began with zero chemiluminescent contributions, to test the validity of this assumption. The EEDF for such plasmas has been extensively studied<sup>76</sup> and is generally modelled as a Maxwell-Boltzmann distribution function with an additional low-intensity high energy tail. The current plasma operates at an electron temperature,  $T_e \sim 1.2$  eV, and the model confirms that none of the variations in process conditions lead to substantial changes in the electron temperature.

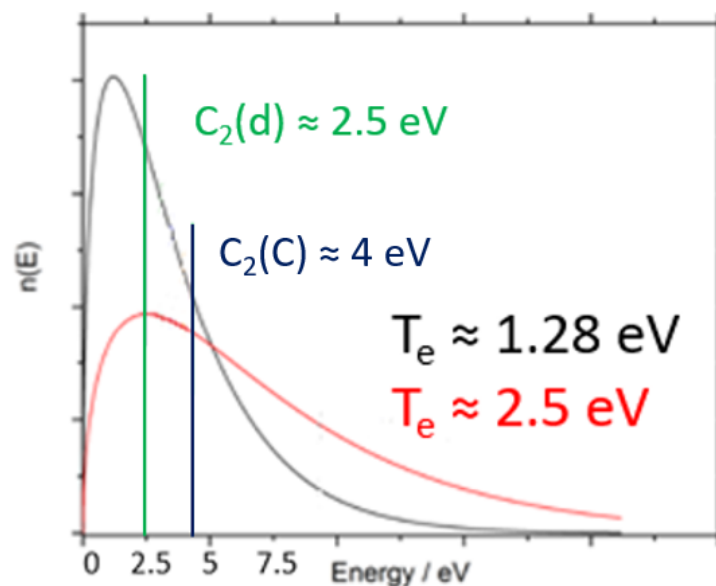


Figure 13: A graph illustrative of the EEDF for two different  $T_e$  values. The lower  $T_e$  value (black curve) is representative of plasma used in the present experiments. The threshold energies for EIE of the d and C states of C<sub>2</sub> are added for illustration.

As can be seen from the Figure 13, a far greater fraction of the electrons have sufficient energy to effect EIE to the lower energy  $C_2(d)$  state than to the  $C_2(C)$ , which can be expected to map through as a significantly lower  $C_2(C)$  state population and lower relative intensity of  $C \rightarrow A$  vs  $d \rightarrow a$  emission – as observed – (typically,  $R_I$  values are around 0.03 at base conditions). Other potential sources of this difference in intensity would be in the emissivities of the respective upper states – the higher energy  $C_2(C)$  has a radiative lifetime roughly 3 times shorter than  $C_2(d)$ , so on average should undergo 3 times fewer collisions than would a  $C_2(d)$  state radical. This would lead to a higher fluorescence quantum yield for  $C_2(C)$  species, which will also be reflected in the  $R_I$  values.

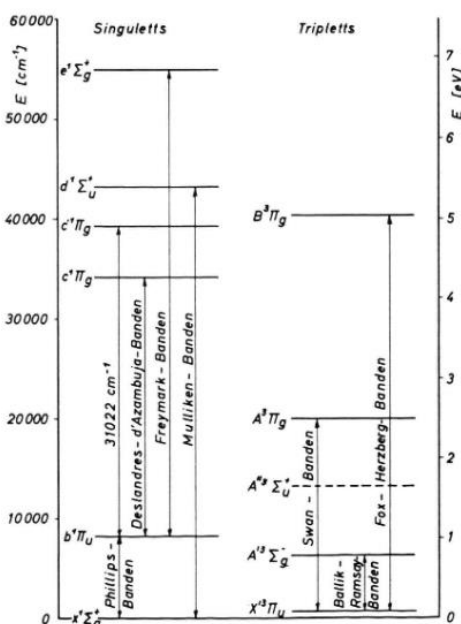


Figure 14: A (rather historic) plot of the electronic energy levels of  $C_2^{77}$ .

As can be observed in Figure 14, other potential radiative decay routes from the states in question are possible which were not directly imaged. However, these would likely be far lower in intensity than anything being directly imaged as they would, for the most part, involve forbidden transitions. For  $C_2(C)$  (shown as c in Figure 14), the only parity-allowed transition is to the A state, and for  $C_2(d)$  (shown as A in Figure 14), the only parity-allowed transition is to the a state (shown as X in Figure 14). In this figure, despite the state labels changing, the state energies have not changed and are still valid. As such, the effects of other radiative decay routes are likely to be extremely minimal, and would not affect the overall intensities of the two emissions selected for this study.

Operating under the traditional assumption that EIE is the sole source of excited species, we would expect that the spatial profile (as a factor of  $z$ ) of  $C_2^*$  would be rather simple; an increase from substrate to the plasma core, followed by a more gradual area decline in intensity as the edge of the plasma is reached and the population of free electrons drastically decreases. As the  $C_2$  dependency on  $p$ , is factored out,  $R_I$  is dependant only on  $n_e$ , and  $T_e$ , which are approximately constant across the plasma core. At high  $z$ ,  $n_e$  drops to zero, so  $R_I$  will also drop to zero.

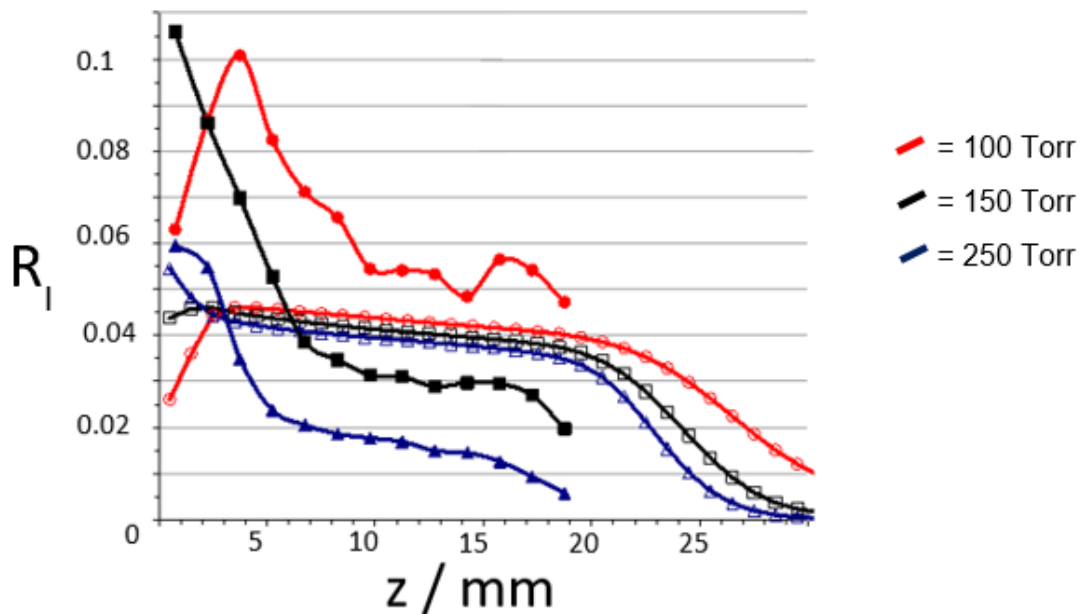


Figure 15: Plots of  $R_I$  vs  $z$ , for three different  $p$ , comparing simulated and experimental results for the EIE-only model.

The expected effects of our three experimental variables ( $p$ ,  $P$  and  $\chi_{CH_4}$ ) would also be relatively straightforward to predict. We would expect that as the overall methane mole fraction ( $\chi_{CH_4}$ ) is increased, the intensity of  $C_2^*$  emission would increase linearly, as  $I_{C_2}$  would be only dependent on  $n_e$ ,  $T_e$ , and the total population of  $C_2$ , which is in turn dependant on the population of  $CH_4$ . The expected effect of increasing  $p$  would be minimal – the equilibria between the various H-shifting reactions would largely be unaffected, and as such we would expect only similar increases to the formation rates of both states, and a roughly equal change in both states. However, increasing  $p$  could potentially increase the quenching rate of the excited states. If the quenching rates for the C and d states are not similar, changing  $p$  might introduce an effect on the dependency of  $R_I$  with  $p$ . Finally, we would expect the effects of increasing power to be similarly minor, providing a small increase in the overall electron temperature

and as such slightly favouring formation of  $C_2(C)$ , though the overall effect would be small.

Once all the experimental data had been taken and plotted, it was compared against a simulation run at identical conditions which assumed that the rate constants of all chemiluminescent reactions were zero. The outputs of these simulations (excited state concentration ratios, proportional to the measured  $R_i$  ratios) were plotted on the same graph as the experimental ratios as a function of  $z$ , which allowed for easy comparison of the EIE-only model with experimental data.

As is shown on Figure 15, the match between experimental (closed symbols) and simulated (open symbols) ratios is poor – neither the shape nor the  $p$  dependences match, especially at low  $z$ . This leads to the conclusion that something is missing from the EIE-only model and encourages exploration of whether inclusion of one or more CL reactions could account for the discrepancies.

### 3.2.3 Potential Chemiluminescent Contributions

Since the match of the experimental data to the EIE-only simulation was so poor, a set of  $C_2$  production/loss mechanisms were then included into the simulation (shown in Table 2).

$i$	Reaction	Rate Coefficient, $k_i$	$R_b / \text{cm}^{-3} \text{s}^{-1}$
3.1	$C_2(a) + e \rightarrow C_2(d) + e$	$9 \times 10^{-9} T_e^{0.5} \exp(-2.5/T_e)$	$7.55 \times 10^{14}$
3.2	$C_2(X) + e \rightarrow C_2(d) + e$	$5.6 \times 10^{-10} T_e^{0.7} \exp(-2.6/T_e)$	$2.35 \times 10^{13}$
3.3	$C_2H_2 + e \rightarrow C_2(d) + 2H + e$	$3.8 \times 10^{-12} T_e^2 \exp(-14/T_e)$	$9.87 \times 10^{10}$
3.4	$C_2(d) \rightarrow C_2(a) + h\nu$	$1.02 \times 10^7$	$7.61 \times 10^{14}$
3.5	$C_2(d) + H_2 \rightarrow C_2H + H$	$1.17 \times 10^{-11}$	$3.32 \times 10^{14}$
-3.5	$C_2H + H \rightarrow C_2(d) + H_2$	$3.0 \times 10^{-12} \exp(-33740/T_{\text{gas}})$	$6.40 \times 10^{14}$
3.6	$C_2(d) + H \rightarrow CH + C(^3P)$	$10^{-10} \exp(-1500/T_{\text{gas}})$	$3.40 \times 10^{14}$
-3.6	$CH + C(^3P) \rightarrow C_2(d) + H$	$10^{-13}$	$2.05 \times 10^{12}$
3.7	$C_2(a) + e \rightarrow C_2(C) + e$	$6.8 \times 10^{-9} T_e^{0.7} \exp(-4.15/T_e)$	$1.46 \times 10^{14}$
3.8	$C_2H_2 + e \rightarrow C_2(C) + H_2 + e$	$1.1 \times 10^{-13} T_e^{0.75} \exp(-12.1/T_e)$	$1.25 \times 10^{10}$
3.9	$C_2(C) \rightarrow C_2(A) + h\nu$	$3.33 \times 10^7$	$3.57 \times 10^{13}$
3.10	$C_2(C) + H_2 \rightarrow C_2H + H$	$1.17 \times 10^{-11}$	$4.77 \times 10^{12}$

-3.10	$C_2H + H \rightarrow C_2(C) + H_2$	$2.55 \times 10^{-12} \exp(-54279/T_{gas})$	$9.50 \times 10^{11}$
3.11	$C_2(C) + H \rightarrow CH + C(^3P)$	$1.4 \times 10^{-9}$	$1.10 \times 10^{14}$
-3.11	$CH + C(^3P) \rightarrow C_2(C) + H$	$7.9 \times 10^{-11} \exp(-19031/T_{gas})$	$3.88 \times 10^{12}$

Table 2: Excited state production and loss reactions included in the best fit simulation, including EIE terms (3.1, 3.2 and 3.7), CL source terms (-3.5, -3.6, -3.10 and -3.11), radiative decay (3.4 and 3.9) and excited state quenching reactions (3.5, 3.6, 3.10 and 3.11) along with their associated rate constants and predicted rates ( $R_b$ ) under base conditions in the centre of the plasma.

$r = 0$ ,  $z = 10.5$  mm, with  $T_e = 1.21$  eV and  $T_{gas} = 3154$  K. Other relevant conditions are a reduced electric field,  $|E|/N = 30.4$  Td,  $n_e = 4.4 \times 10^{11} \text{ cm}^{-3}$  and  $[H] = 7.4 \times 10^{16} \text{ cm}^{-3}$ . The rate coefficients,  $k_i$  are in units of  $\text{cm}^3 \text{ s}^{-1}$ , except for radiative decays (reactions 3.4 and 3.9), where the units are  $\text{s}^{-1}$ .

Whilst it is true that since  $C_2(C)$  is higher in energy these reactions would be mostly faster (sometimes being barrierless whereas one  $C_2(d)$  reaction (3.6) is shown as having a small barrier), the temperature at which these reactions would be occurring (roughly 2500 K) would mean that for all intents and purposes these collisions are >95% efficient, meaning that the only appreciable difference in non-radiative decay is due to the longer radiative lifetime of  $C_2(d)$ , whether the eventual non-radiative decay is purely collisional or bimolecular is unimportant for our study.

As is evident from the rate constants, CL reactions are more favourable overall for producing the lower energy  $C_2(d)$  state (difference between the predicted rates of reactions -3.5 and -3.10 is  $\approx 673$ ) due to the smaller activation barrier to the former. This is also true for EIE reactions as well (difference between reactions 3.1 and 3.7 is  $\approx 5.2$ ), which agrees with expectations (detailed in section 3.2.2). For the d state, the highest rate of loss is by radiative loss (reaction 3.4), followed by bimolecular collision with hydrogen (reaction 3.6), whereas for the C state, collision with hydrogen (reaction 3.11) is predicted to have a higher rate than radiative loss (reaction 3.9). For both species, collision with hydrogen is by far the major route of non-radiative loss. This is expected as  $H_2$  is by a long way the most abundant species within the reactor, so should be the majority collision partner. This goes some way to explaining the pressure dependency of  $R_i$ , as the higher pressure would unevenly affect the non-radiative loss of the C state more than the d state due to the

difference in primary loss route. Also of note is the dominance of the  $\text{H} + \text{C}_2\text{H} \rightarrow \text{C}_2 + \text{H}_2$  reaction (reactions -3.5 and -3.10) as the dominant CL source of  $\text{C}_2^*$  over other potential reactions, which are mentioned further later in this section. However, reaction -3.5 (d state) is responsible for approximately 45% of total  $\text{C}_2(\text{d})$  formation in this model, but reaction -3.10 (C state) is only responsible for approximately 0.6% of  $\text{C}_2(\text{C})$  formation. This agrees with our previous suggestion that the d state would have a significant CL source, but the C state would be formed nearly fully by EIE reactions. This reaction scheme would imply a far greater dependence on  $T_{\text{gas}}$  than in the EIE-only model (covered by reactions 3.1, 3.2, 3.3, 3.7, and 3.8), thus indicating a greater dependence on  $z$  than previously modelled, which explains the poor fitting of the old model to the experimental results and works well with the  $z$ -dependencies shown in Figures 10-12.

As with the OES measurements (Figure 15), the 2-D model predicts no serious dependences of  $R_I$  with  $\chi_{\text{CH}_4}$ . The values of  $T_{\text{gas}}$  and  $T_e$  only slightly increase with increases to  $\chi_{\text{CH}_4}$ , causing a very minor increase in  $R_I$ .

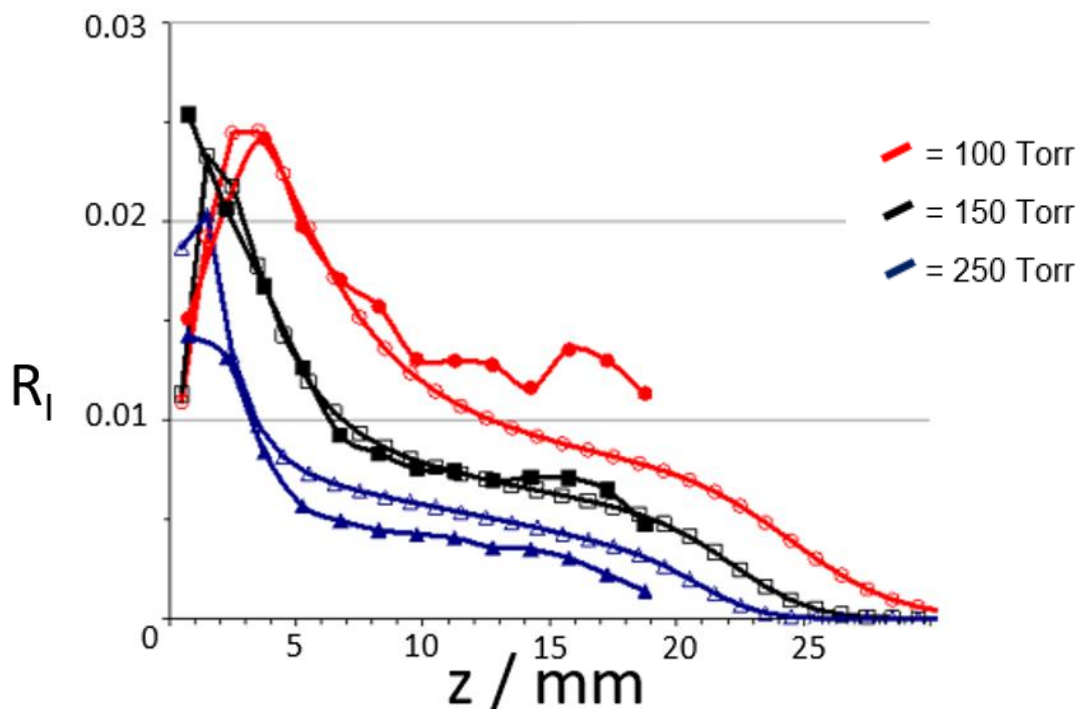


Figure 16: Plots of  $R_I$  vs  $z$ , for three different  $p$ , comparing simulated and experimental results for the EIE+CL+ excited state quenching model parametrized in table 2.

In the case of pressure dependency, the reaction mechanisms detailed in Table 2 provide good correlation with the respective  $R_I$  profiles at all pressures. Increasing pressure will lead to a reduction in the plasma volume and an associated increase in  $T_{gas}$ , increasing the rate of reaction 1.1 and so increasing [H]. This will primarily affect the relative rates of the fluorescence quenching reactions (3.6 and 3.11). This will lead to preferential quenching of  $C_2(C)$ , leading to a reduction in  $R_I$ , which can be observed in Figure 10.

Increasing power only produces a small effect on  $T_e$ , and  $T_{gas}$ , resulting in a small decrease in  $T_{gas}$  and a small increase in  $T_e$  when the power is increased. As with pressure, this increase in  $T_e$  will result in an increase in  $R_I$ , though no major power dependency is shown.

As is immediately obvious from Figure 16, the inclusion of this reaction scheme, summarized in Table 2, including CL reactions dramatically improves the fitting of the experimental to the simulations.

Whilst some other potential reactions for CL formation of  $C_2$  were considered, such as  $CH + CH \rightarrow C_2 + H_2$  and  $C + CH_2 \rightarrow C_2 + H_2$ , upon further investigation neither of these reactions are expected to be competitive with the rates of reactions -3.5 and -3.10. These reactions involve the collision of reactants that are in far lower populations within the plasma core, and as such the far lower collision rate will significantly outweigh the higher collisional efficiency of these reactions.

#### 4. Conclusions and Further Work

It can be concluded from this work that the traditional assumption that EIE is the only important route of forming  $C_2^*$  is incorrect, and that – as in the case of CH emissions from MW activated C/H gas mixtures - CL reactions play a significant role in the formation of excited state  $C_2$  radicals – particularly  $C_2$  radicals in the lower lying d state. This is clearly shown by the dramatically better fit of the experimental data when CL sources are included with simulation, and the very poor match between EIE-only simulations with the same experimental data.

Further work could entail adding a significant argon fraction, replacing half or more of the hydrogen flow with argon to approach conditions used for growing nano- or even ultranano-crystalline diamond. Substantial Ar emissions would drive up  $T_{gas}$  as the

rate of diffusive heat transfer declines, leading to an increased degree of H<sub>2</sub> dissociation and higher [H]. Increasing  $T_{gas}$  would be expected to further favour CL contributions and may allow other minor C<sub>2</sub> forming reactions to take place.

Other studies could investigate doped systems further, especially C/H plasmas including trace additions of B (and Si). This would allow investigation into CL reactions to form boron- and silicon-containing species that are key in the doping process, potentially allowing dramatic improvements to both the speed and consistency of doping with these species by altering and optimizing doping conditions.

Potential study could be repeated for other gas activation techniques, such as plasma jet systems. This could provide new insights as to the differences between the plasma excitation techniques and would also serve to further confirm the presence of major CL contributions.

More study into other carbon containing species is also fundamentally possible, though this would require another carbon-containing species that is present in appreciable concentration and has two readily emitting states with meaningful differences in energy and both of the states being observable on the same equipment to allow for more study into CL contributions to other reactions. If this is not feasible, runs could be completed to assess the CL contributions to other carbon-containing species – such as C<sub>3</sub>, which has an excited A state that emits at ~405 nm, by using the C<sub>2</sub>(C) state, for example, to inform on the electron conditions within the reactor (mainly  $T_{gas}$  and  $T_e$ ), then using these conditions to discern the difference between EIE formation only population of a species and the actual total population of that species.

## 5. References

- 1) Diamonds Price Index, <https://www.diamondse.info/diamonds-price-index.asp/>, (Last accessed April 2020).
- 2) Statista global rough diamond production, <https://www.statista.com/statistics/274921/worldwide-production-of-rough-diamonds/>, (Last accessed April 2020).
- 3) Statista global synthetic diamond production <https://www.statista.com/statistics/280216/global-synthetic-diamond-production/>, (Last accessed April 2020).

- 4) Mordor Intelligence synthetic diamond market – growth, trends and forecast <https://www.mordorintelligence.com/industry-reports/synthetic-diamond-market/>, (Last accessed April 2020).
- 5) W. A. Weimer and C. E. Johnson, presented in part at the 34<sup>th</sup> Annual International Technical Symposium on Optical and Optoelectronic Applied Science and Engineering, December, 1990.
- 6) F. P. Bundy, H. T. Hall, H. M. Strong and R. H. Wentorf, *Nature*, 1955, **176**, 51-55.
- 7) J. C. Angus, *Diam. Relat. Mater.*, 2014, **49**, 77-86.
- 8) J. E. Butler, Y. A. Mankelevich, A. Cheesman, J. Ma and M. N. R. Ashfold, *J. Phys. : Condens. Matter*, 2009, **36**, 364201.
- 9) E. J. D. Mahoney, PhD Thesis, University of Bristol, 2019.
- 10) Hexa research global synthetic diamond market revenue by process <https://www.hexaresearch.com/research-report/synthetic-diamond-market/>, (Last accessed April 2020).
- 11) P. M. Martineau, M. P. Gaukroger, K. B. Guy, S. C. Lawson, D. J. Twitchen, I. Friel, J. O. Hansen, G. C. Summerton, T. P. G. Addison, and R. Burns, *J. Phys. : Condens. Matter*, 2009, **36**, 364205.
- 12) Y. Mokuno, A. Chayahara, H. Yamada, and N. Tsubouchi, *Diam. Relat. Mater.*, 2009, **10**, 1258-1261.
- 13) J. V. Busch, J. P. Dismukes, V. N. Narllicheri and K. R. Walton, *Mater. Sci. Monogr.*, 1991, **73**, 623-633.
- 14) P.W. May, *Phil. Trans. R. Soc. Lond. A*, 2000, **358**, 473-495 .
- 15) J.E. Graebner, in *Diamond: Electronic Properties and Applications*, ed. L.S. Pan and D.R. Kania, Springer, Boston, 1995, ch. 7, pp. 285-318.
- 16) Chemistry World article Diamonds are for Everything <https://www.chemistryworld.com/features/diamonds-are-for-everything/3004568.article/> (last accessed April 2020).
- 17) K. Kanda, S. Takehana, S. Yoshida, R. Watanabe, S. Takano, H. Ando, and F. Shimakura. *Surf. Coat. Technol.*, 1995, **73**, 115-120.
- 18) M. Labudovic and M. Burka, *IEEE T. Compon. Pack. T.*, 2003, **26**, 575-581.
- 19) M. W. Geis, D. D. Rathman, D. J. Ehrlich, R. A. Murphy, and W. T. Lindley, *IEEE Electr. Device L.*, 1987, **8**, 341-343.
- 20) Y. Tzuk, A. Tal, S. Goldring, Y. Glick, E. Lebuish, G. Kaufman and R. Lavi, *IEEE J. Quantum Elect.*, 2004, **40**, 262-269 .
- 21) K. Sakamoto, A. Kasugai, M. Tsuneoka, K. Takahashi, T. Imai, T. Kariva and Y. Mitsunaka, *Rev. Sci. Instrum.*, 1999, **70**, 208-212.

- 22) C. Moelle, S. Klose, F. Szücs, H. J. Fecht, C. Johnston, P. R. Chalker, and M. Werner, *Diam. Relat. Mater.*, 1997, **6**, 839-842.
- 23) R. Kalish, *Carbon*, 1999, **37**, 781-785.
- 24) V. S. Vavilov and E. A. Konorova, *Sov. Phys. Uspekhi*, 1976, **19**, 301.
- 25) K. J. Russell and William J. Leivo, , *Phys. Rev. B*, 1972, **6**, 4588.
- 26) K. Okano, H. Kiyota, T. Iwasaki, Y. Nakamura, Y. Akiba, T. Kurosu, M. Iida and T. Namakumra, *App. Phys. A*, 1990, **51**, 344-346.
- 27) J. Isberg, J. Hammersberg, E. Johansson, T. Wilkström, D. J. Twitchen, A. J. Whitehead, S. E. Coe and G. A. Scarsbrook, *Science*, 2002, **297**, 1670-1672.
- 28) H. Taniuchi, H. Umezawa, T. Arima, M. Tachiki and H. Kawarada, *IEEE Electr. Device L.*, 2001, **22**, 390-392.
- 29) S. Dhomkar, J. Henshaw, H. Jayakumar and C. A. Meriles, *Sci. Adv.*, 2016, **2**, e1600911.
- 30) J. Hornstra, *J. Phys. Chem. Solids*, 1958, **5**, 129-141.
- 31) W. F. Banholzer and T. R. Anthony, *Thin Solid Films*, 1992, **212**, 1-10.
- 32) J. J. Gracio, Q. H. Fan and J. C. Madaleno, *J. Phys. D Appl. Phys.*, 2010, **43**, 374017.
- 33) Mindat diamond data page, <https://www.mindat.org/min-1282.html>, (last accessed April 2020).
- 34) Mindat graphite data page, <https://www.mindat.org/min-1740.html>, (last accessed April 2020).
- 35) D. Choudhary and J. Bellare, *Ceram. Int.*, 2000, **26**, 73-85.
- 36) M. Akaishi, *Diam. Relat. Mater.*, 1993, **2**, 183-189.
- 37) R. P. Dias and I. F. Silvera. *Science*, 2017, **355**, 715-718.
- 38) J. Hirmke, S. Schwarz, C. Rottmair, S. M. Rosiwal, and R. F. Singer, *Diam. Relat. Mater.*, 2006, **15**, 536-541.
- 39) J. J. Lander and J. Morrison, *Surf. Sci.*, 1966, **4**, 241-246.
- 40) B. V. Spitsyn, L. L. Bouilov and B. V. Derjaguin, *J. Cryst. Growth*, 1981, **52**, 219-226
- 41) S. Nad, PhD Thesis, Michigan State University, 2016
- 42) S. Matsumoto, Y. Sato, M. Tsutsumi and N. Setaka, *J. Mater. Sci.*, 1982, **17**, 3106–3112.
- 43) M. Schwander and K. Partes, *Diam. Relat. Mater.*, 2011, **20**, 1287-1301.
- 44) P. W. May, W., C. A. Rego, R. M. Thomas, M. N. R. Ashfold, K. N. Rosser, and N. M. Everitt, *Diam. Relat. Mater.*, 1994, **3**, 810-813.

- 45) L. M. Hanssen, W. A. Carrington, J. E. Butler, and K. A. Snail, *Mater. L.*, 1988, **7**, 289-292.
- 46) G. Janssen, W. J. P. Van Enckevort, J. J. D. Schaminee, W. Vollenberg, L. J. Giling, and M. Seal, *J. Cryst. Growth*, 1990, **104**, 752-757.
- 47) D. G. Goodwin, *Appl. Phys. L.*, 1991, **59**, 277-279.
- 48) J. A. Smith, K. N. Rosser, H. Yagi, M. I. Wallace, P. W. May, and M. N. R. Ashfold, *Diam. Relat. Mater.*, 2001, **10**, 370-375.
- 49) C. J. Rennick, J. A. Smith, M. N. R. Ashfold, and A. J. Orr-Ewing, *Chem. Phys. L.*, 2004, **383**, 518-522.
- 50) J. Petherbridge, PhD Thesis, University of Bristol, 2002
- 51) J. Alden, MSc Thesis, University of Bristol, 2019
- 52) Z. Yiming, F. Larsson, and K. Larsson, *Theor. Chem. Acc.*, 2014, **133**, 1432.
- 53) S. Jin and T. D. Moustakas, *Appl. Phys. L.*, 1994, **65**, 403-405.
- 54) T. Kawato and K. Kondo, *Jap. J. Appl. Phys.*, 1987, **26**, 1429.
- 55) J. Mort, D. Kuhman, M. Machonkin, M. Morgan, F. Jansen, K. Okumura, Y. M. LeGrice, and R. J. Nemanich, *Appl. Phys. L.*, 1989, **55**, 1121-1123.
- 56) J. Zhang, X. Wang, B. Shen and F. Sun, *Int. J. Refract. Met. H.*, 2013, **41**, 285-292.
- 57) S. Koizumi, T. Teraji, and H. Kanda, *Diam. Relat. Mater.*, 2000, **9**, 935-940.
- 58) E. Gheeraert, A. Deneuville, and J. Mambou, *Carbon*, 1999, **37**, 107-111.
- 59) A. Tallaire, C. Rond, F. Benedic, O. Brinza, J. Achard, F. Silva, and A. Gicquel, *Phys. Status Solidi A*, 2011, **208**, 2028-2032.
- 60) J. Ma J. C. Richley, M. N. R. Ashfold, and Y. A. Mankelevich, 2008, *J. Appl. Phys.*, **104**, 10305.
- 61) F. G. Celii and J. E. Butler, *J. Appl. Phys.*, 1992, **71**, 2877-2883.
- 62) K. M. McNamara, B. E. Williams, K. K. Gleason, and B. E. Scruggs, *J. Appl. Phys.*, 1994, **76**, 2466-2472.
- 63) R. W. Bormett, S. A. Asher, R. E. Witowski, W. D. Partlow, R. Lizewski, and F. Pettit, *J. Appl. Phys.*, 1995, **77**, 5916-5923.
- 64) R. S. Tsang, C. A. Rego, P. W. May, M. N. R. Ashfold, and K. N. , *Diam. Relat. Mater.*, 1997, **6**, 247-254.
- 65) A. N. Goyette, J. E. Lawler, L. W. Anderson, D. M. Gruen, T. G. McCauley, D. Zhou, and A. R. Krauss, *Plasma Sources Sci. T.*, 1998, **7**, 149.
- 66) A. Inspektor, Y. Liou, T. McKenna, and R. Messier, *Surf. Coat. Technol.*, 1989, **39**, 211-221.
- 67) C. F. Chabalowski, S. D. Peyerimhoff and R. J. Buenker, *Chem. Phys.*, 1983, **81**, 57-72.

- 68) J. Cui and R. Fang, *J. Appl. Phys.*, 1997, **81**, 2856-2862.
- 69) J. W. Coburn and M. Chen, *J. Appl. Phys.*, 1980, **51**, 3134-3136.
- 70) Y. A. Mankelevich and P. W. May, *Diam. Relat. Mater.*, 2008, **17**, 1021-1028.
- 71) NIST chemistry webbook dicarbon constants, <https://webbook.nist.gov/cgi/cbook.cgi?Formula=c2&Nolon=on&Units=SI&cDI=on/>, (last accessed April 2020).
- 72) J. E. Mentall and R. W. Nicholls, *Proc. Phys. Soc.*, 1965, **86**, 873.
- 73) J. S. Brooke, P. F. Bernath, T. W. Schmidt and G. B. Bacskay, *J. Quant. Spectrosc. Radiat. Transf.*, 2013, **124**, 11-20.
- 74) Andor Newton 940 specs sheet, <https://andor.oxinst.com/products/newton-ccd-and-emccd-cameras/newton-940/>, (last accessed April 2020).
- 75) Richardson gratings specs sheet, [https://www.gratinglab.com/Products/Product\\_Tables/Efficiency/Efficiency.aspx?catalog=53\\*-455R/](https://www.gratinglab.com/Products/Product_Tables/Efficiency/Efficiency.aspx?catalog=53*-455R/), (last accessed April 2020)
- 76) E. J. D. Mahoney, S. Mushtaq, M. N. R. Ashfold and Y. A. Mankelevich, *J. Phys. Chem. A*, 2019, **123**, 2544-2558.
- 77) G. Messerle and L. Krauss, *Z. Naturforschung A*, 1967, **22**, 2015-2023.

## 6. Appendices

### 6.1 MATLAB Calibration

MATLAB calibration was performed using a custom-written program (source code is available upon request). This program has built-in variables to correct for boundary measurements, intensity and fitting, and allows specific region analysis for areas of interest. The inputted spectrum is adjusted by steps of 0.005 in vertical and horizontal axes to correct for baseline variations, and is then binned into either 10×3 mm wide strips or 20×1.5 mm wide strips along the vertical ( $z$ ) axis. Each strip is then plotted against wavelength, outputting either 10 or 20 comma-separated value files which can then be analysed by PGOPHER.

### 6.2 PGOPHER Fitting

PGOPHER simulation was performed by first building two simulations – one containing the C<sub>2</sub> Swan band and then C<sub>2</sub><sup>-</sup> Herzberg-Lagerqvist system (referred to as P<sub>530</sub>), and the other containing the C<sub>2</sub> DD band and the CH(B-X) system (referred to as P<sub>410</sub>). Both simulations were performed at normalized intensity units. Detailed information of the constants used for these simulations is available upon request.

Fitting was performed by first selecting 3 peaks to calibrate from in the experimental data, then using the locations of the peaks within the simulation to calibrate them (Figure App.1). After this, the overlay section was used to adjust the units to Normalized (Figure App.2). Other corrections were then applied, such as allowing the FrequencyOffset and FrequencyScale to float, setting the scale to 1e-8, setting the units to Normalized and setting FixCentre to True (Figure App.3). Finally, a 4-factor polynomial intensity correction was applied and allowed to float (Figure App.4).

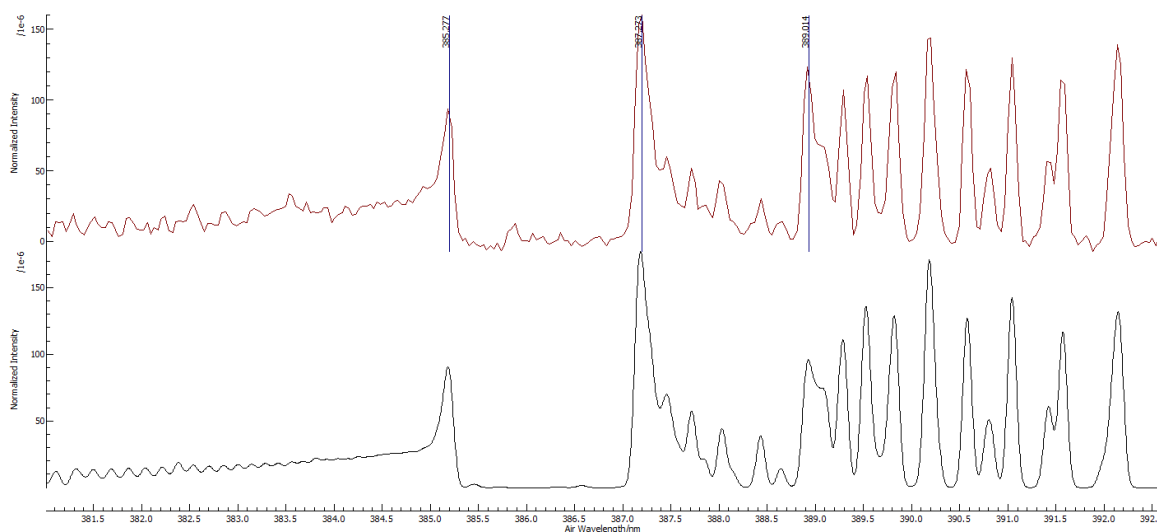


Figure App.1: Calibration of a PGOPHER simulation

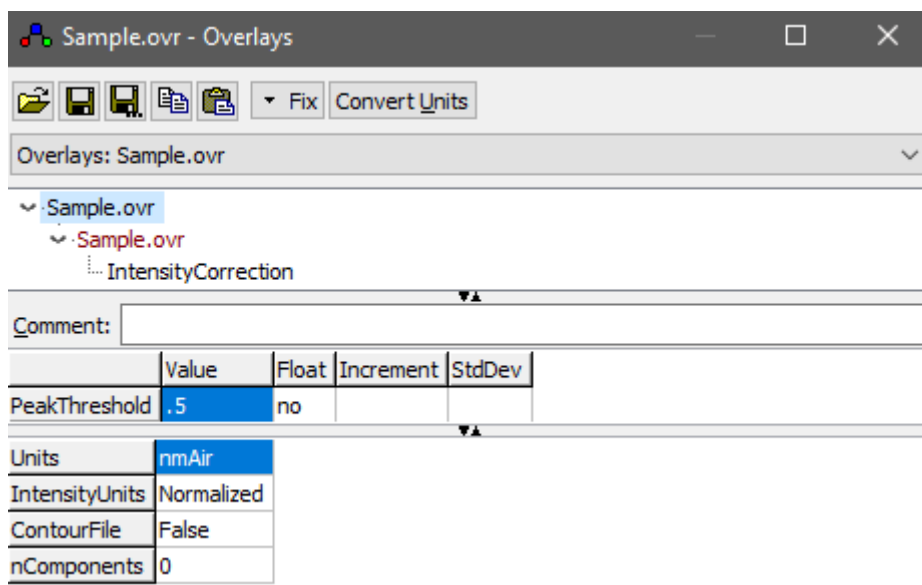


Figure App.2: Page 1 of the Overlays window after adjustments

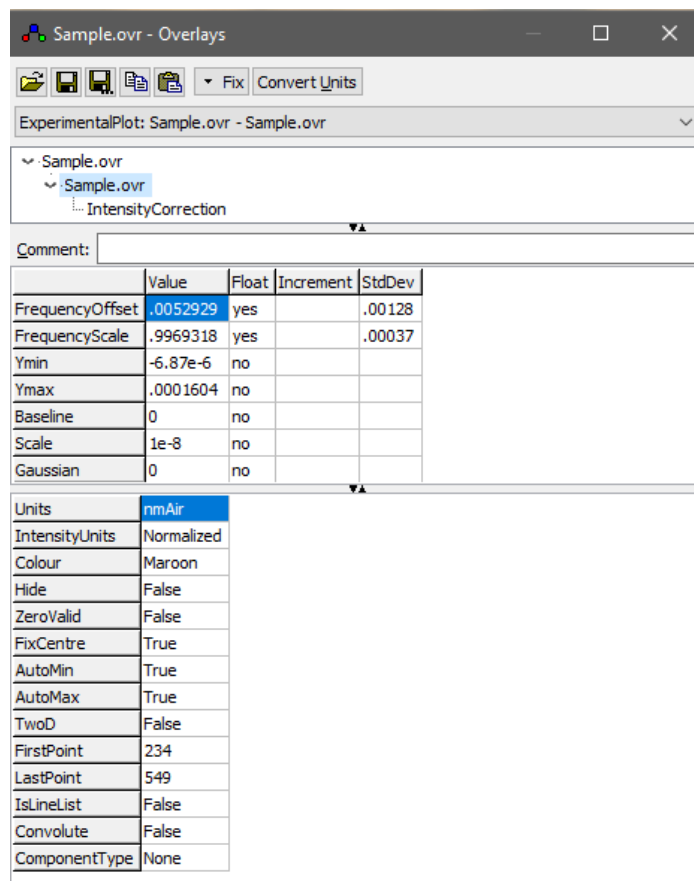


Figure App.3: Page 2 of the Overlays window after adjustments

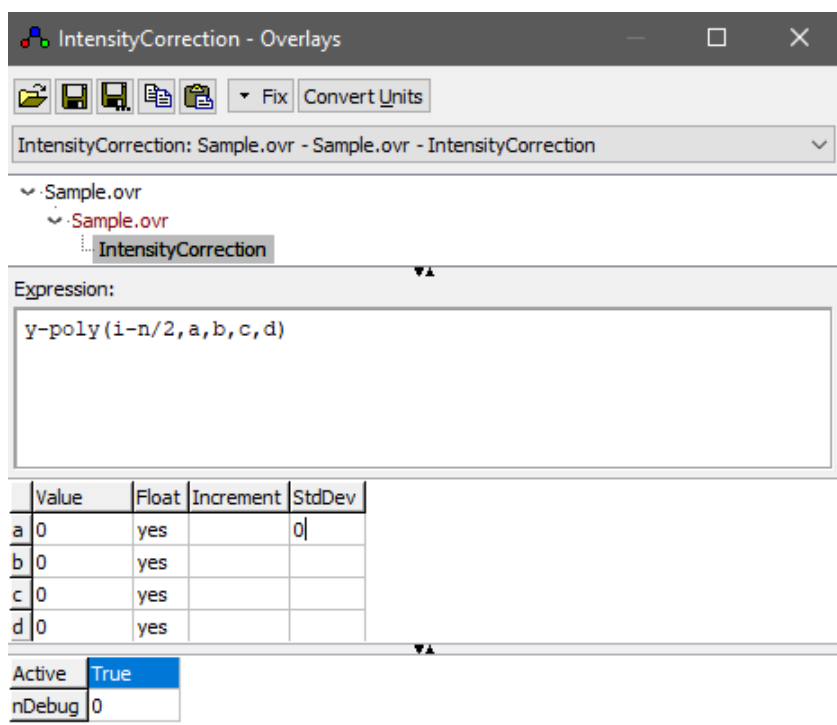


Figure App.4: Page 3 of the Overlays window, showing the intensity correction polynomial.

### 6.3 Experimental Graphs

For all graphs, the y-axis refers to intensity of the labelled species and all labels in units of mm are  $z$ .

#### 6.3.1: Spatial Profiles

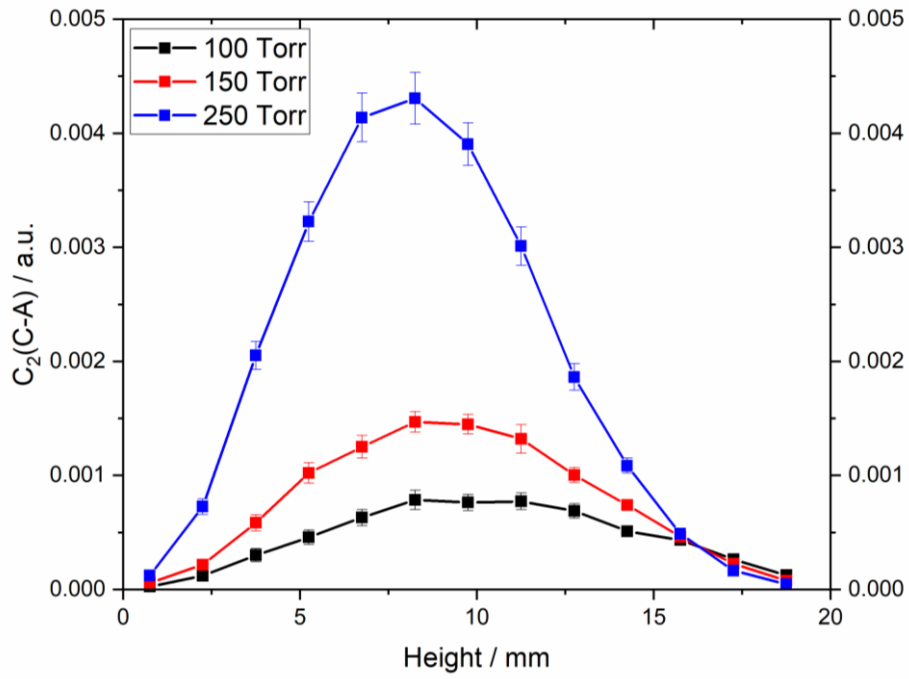


Figure App.5: Spatial profile of  $C_2(C-A)$  at a range of pressures.

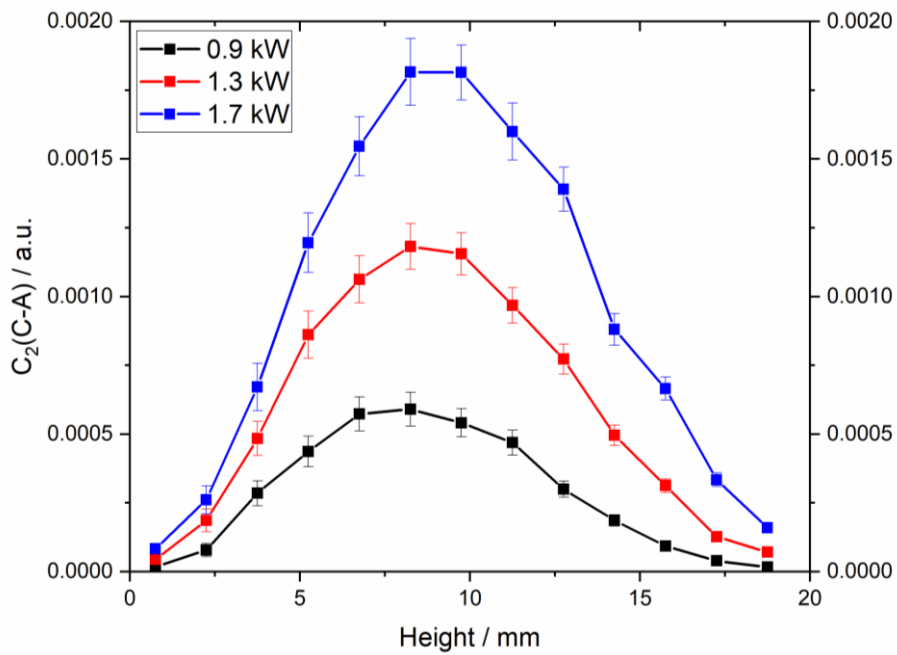


Figure App.6: Spatial profile of  $C_2(C-A)$  at a range of powers.

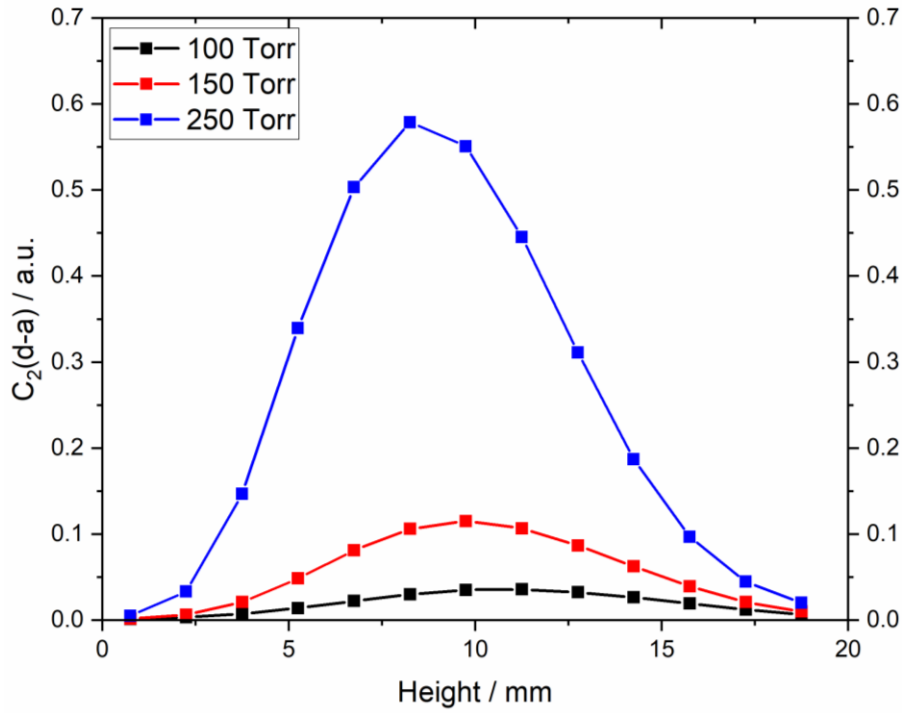


Figure App.7: Spatial profile of  $C_2(d-a)$  at a range of pressures.

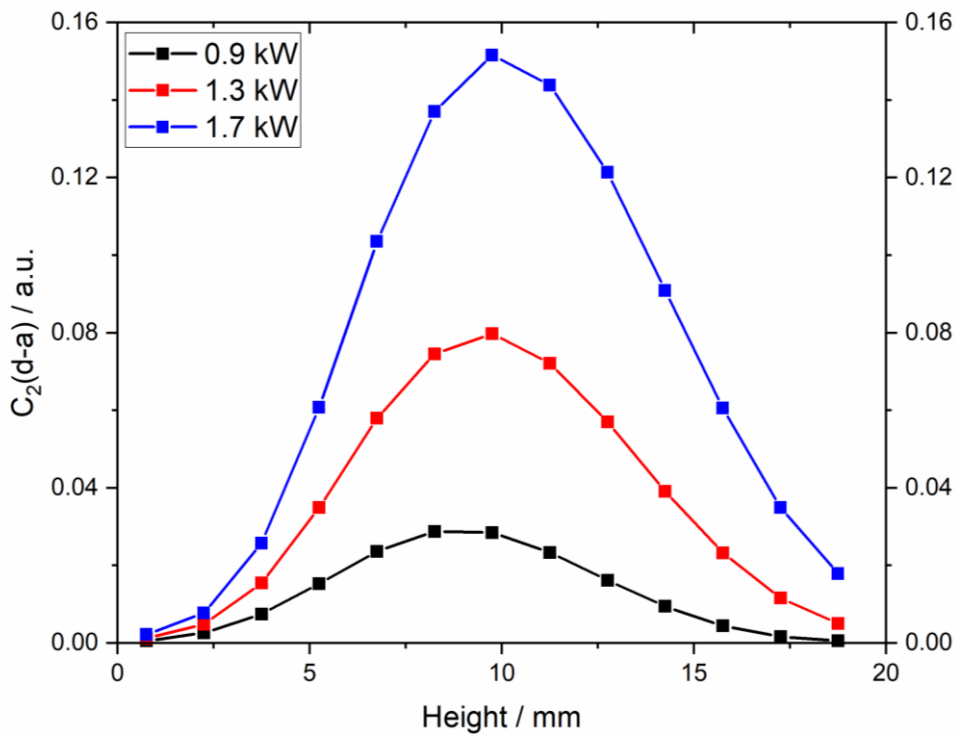


Figure App.8: Spatial profile of  $C_2(d-a)$  at a range of powers.

6.3.2: By Process Conditions

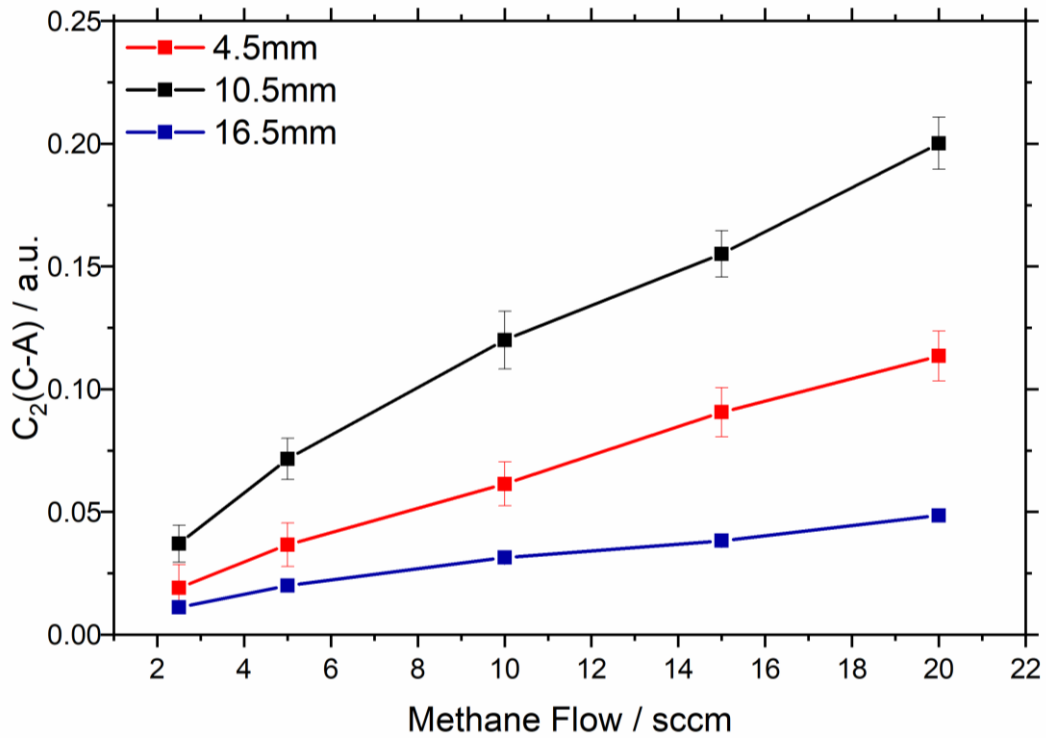


Figure App.9: A graph of C<sub>2</sub>(C-A) vs methane flow.

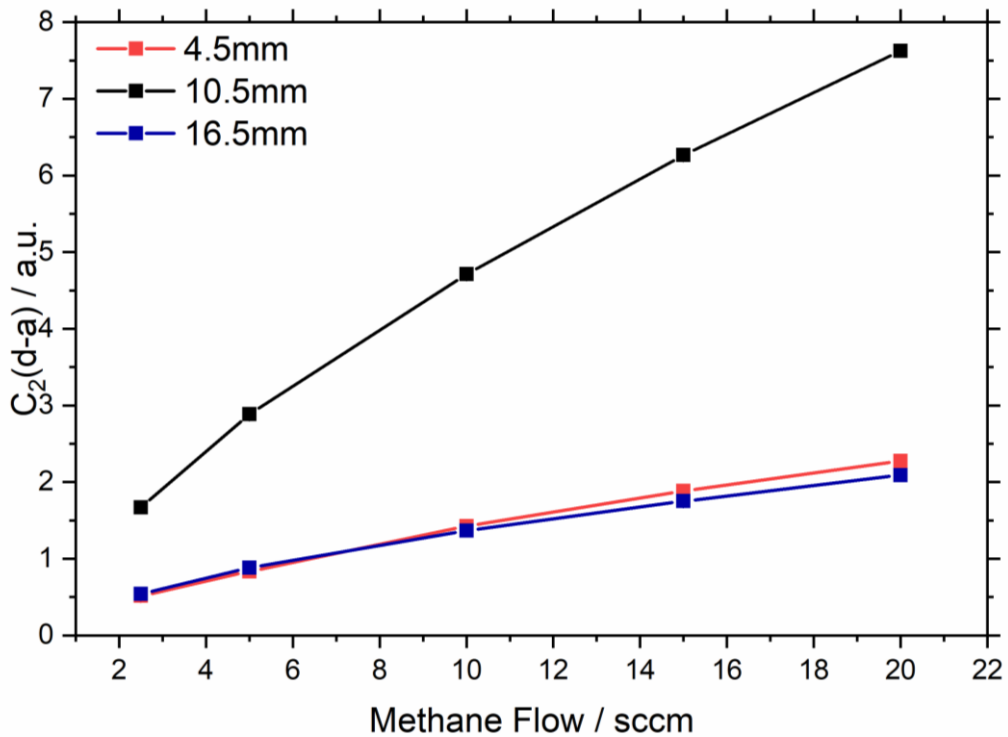


Figure App.10: A graph of C<sub>2</sub>(d-a) vs methane flow.

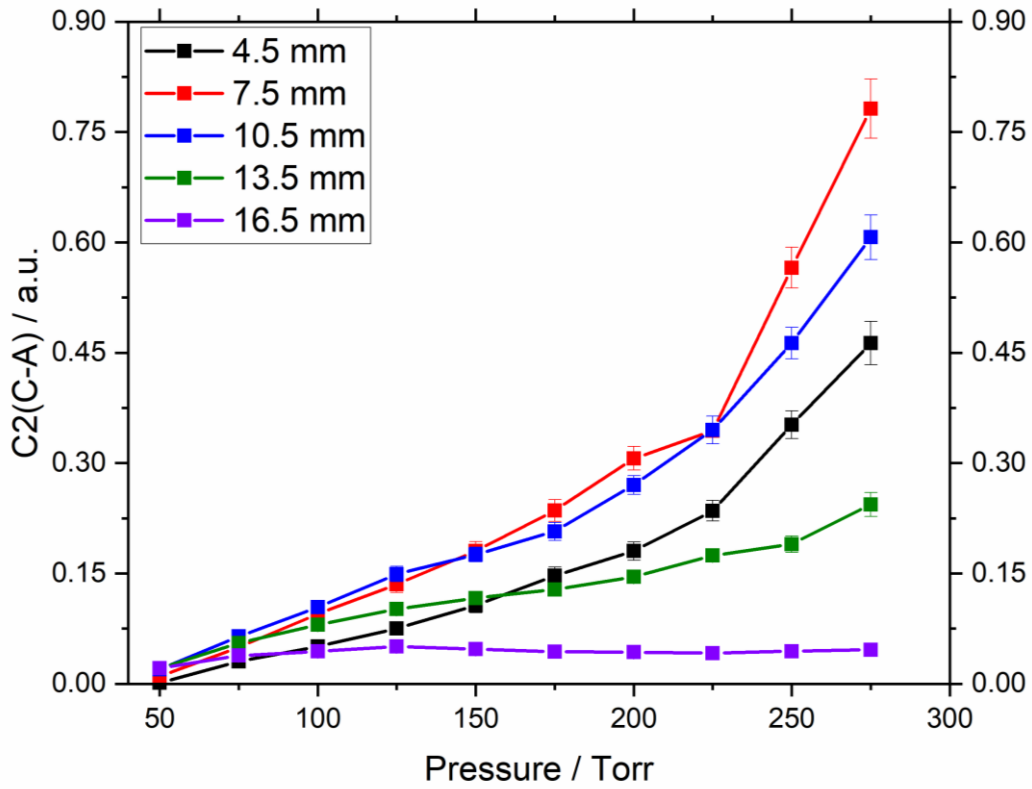


Figure App.11: A graph of C<sub>2</sub>(C-A) vs pressure.

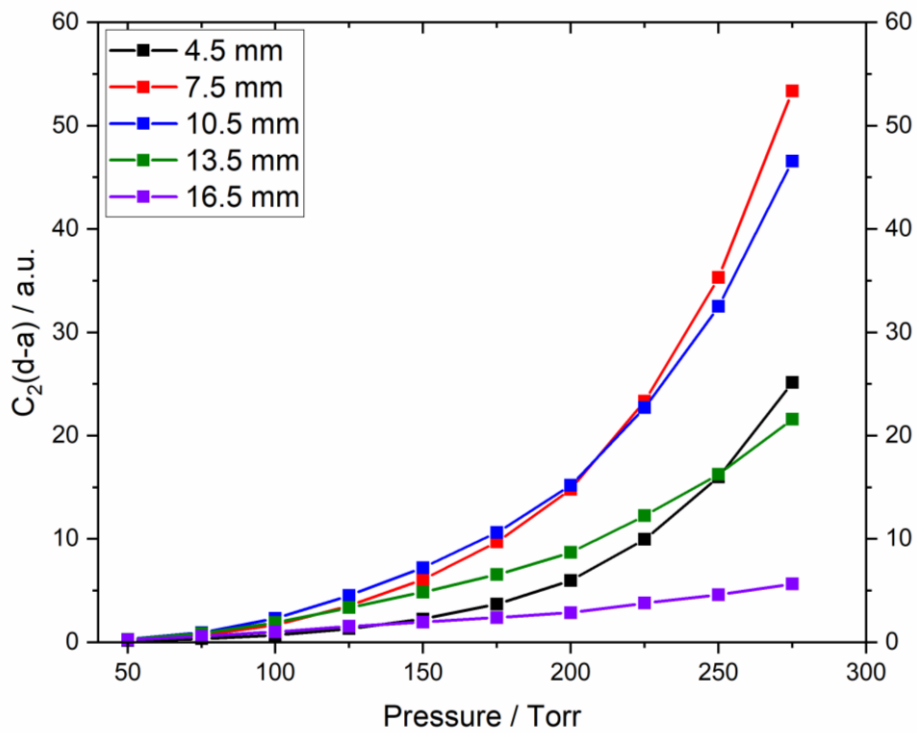


Figure App.12: A graph of C<sub>2</sub>(d-a) vs pressure.

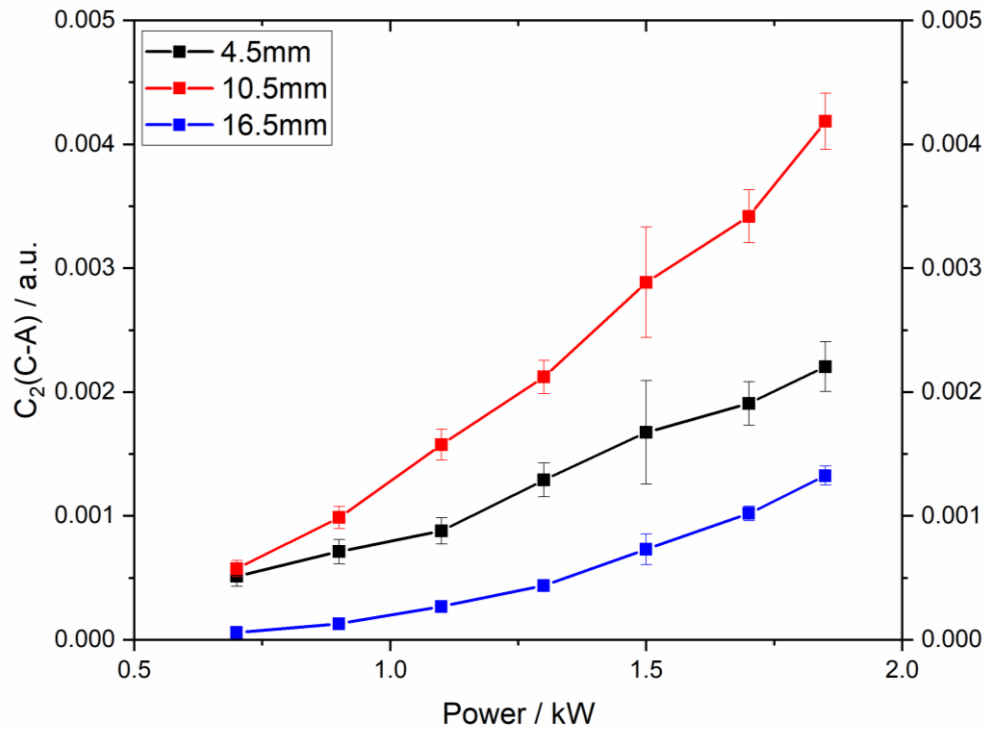


Figure App.13: A graph of C<sub>2</sub>(C-A) vs power.

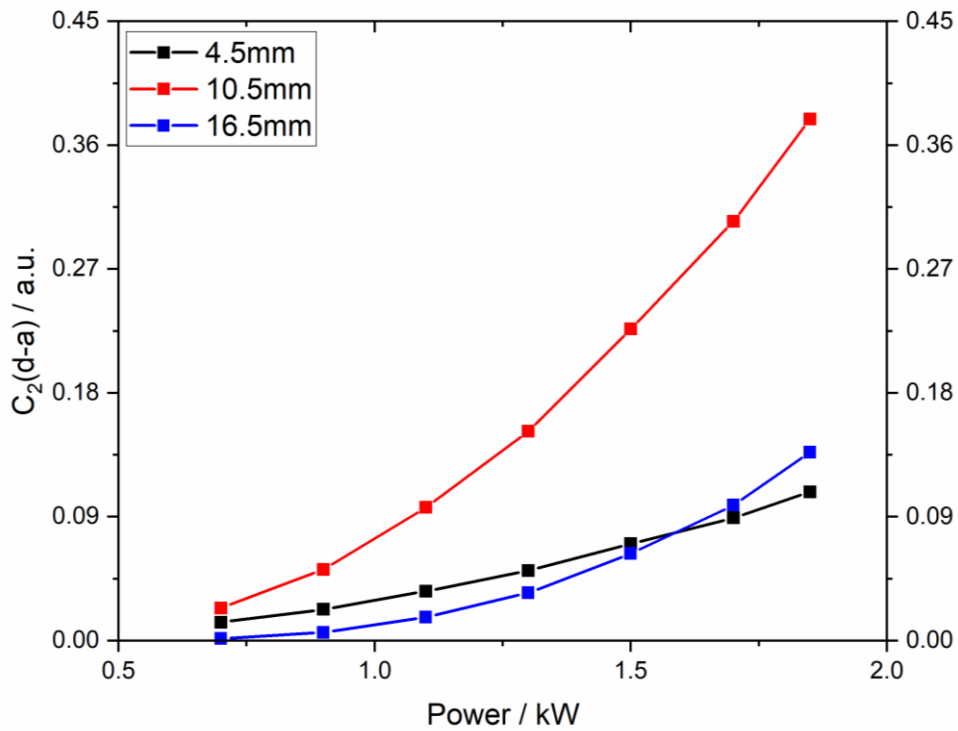


Figure App.14: A graph of C<sub>2</sub>(d-a) vs power.